

# Reduced modeling and global instability of finite-Reynolds-number flow in compliant rectangular channels

Xiaojia Wang, Ivan C. Christov

*School of Mechanical Engineering, Purdue University, West Lafayette, Indiana, 47907, USA*

February 24, 2022

## Contents

<b>1</b>	<b>Introduction</b>	<b>2</b>
<b>2</b>	<b>Problem statement</b>	<b>4</b>
<b>3</b>	<b>Fluid mechanics problem formulation</b>	<b>6</b>
3.1	Scaling and identification of the dominant effects . . . . .	6
3.2	Reduction: lubrication approximation . . . . .	6
<b>4</b>	<b>Solid mechanics problem formulation</b>	<b>7</b>
4.1	Scaling and identification of the dominant effects . . . . .	7
4.2	Reduction: introducing the width-averaged (effective) height . . . . .	8
4.3	Extension: introducing weak deformation effects . . . . .	9
4.3.1	Effective interface thickness . . . . .	9
4.3.2	Weak tension . . . . .	10
4.4	Nondimensionalization: introducing the FSI parameter . . . . .	11
<b>5</b>	<b>Fluid–solid coupling: A new 1D FSI model</b>	<b>12</b>
5.1	Exemplar cases and preview of results . . . . .	14
<b>6</b>	<b>Base state: features of the inflated microchannel at steady state</b>	<b>14</b>
<b>7</b>	<b>Linear stability of the inflated base state</b>	<b>18</b>
7.1	Eigenspectra of the exemplar cases . . . . .	19
7.2	Eigenfunctions of the exemplar cases . . . . .	21
<b>8</b>	<b>Dynamic response of the microchannel</b>	<b>21</b>
8.1	Evolution from a perturbed inflated state . . . . .	23
8.2	Evolution from a flat initial state . . . . .	24
<b>9</b>	<b>Conclusion</b>	<b>26</b>
<b>A</b>	<b>Long-time simulation of the evolution from a perturbed inflated state</b>	<b>28</b>

## Abstract

Experiments have shown that flow in compliant microchannels can become unstable at a much lower Reynolds number than the corresponding flow in a rigid conduit. Therefore, it has been suggested that the wall’s elastic compliance can be exploited towards new modalities of microscale mixing. While previous studies mainly focused on the local instability induced by the fluid–structure interactions (FSIs) in the system, we derive a new one-dimensional (1D) model to study the FSI’s effect on the global instability. The proposed 1D FSI model is tailored to long, shallow rectangular microchannels with a deformable top wall, similar to the experiments. Going beyond the usual lubrication flows analyzed in these geometries, we include finite fluid inertia and couple the reduced flow equations to a reduced 1D wall deformation equation. Although a quantitative comparison to previous experiments is quite difficult, the behaviors of the proposed derived model show qualitative agreement with the experimental observations, and capture several key effects. Specifically, we find the critical conditions under which the inflated base state of the 1D FSI model is linearly unstable to infinitesimal perturbations. The critical Reynolds numbers predicted are in agreement with experimental observations. The unstable modes are highly oscillatory, with frequencies close to the natural frequency of the wall, suggesting that the observed instabilities are resonance phenomena. Furthermore, during the start-up from an undeformed initial state, self-sustained oscillations can be triggered due to FSIs. Our proposed modeling framework can be applied to other microfluidic systems with similar geometric scale separation, even under different operation conditions.

## 1 Introduction

Soft materials, such as elastomers, are used to fabricate microfluidic devices (Sackmann et al., 2014). Consequently, fluid–structure interactions (FSIs) between the compliant walls and the fluids conveyed within such micro-conduits have emerged as a fundamental mechanics problem to understand (Christov, 2022). Previous studies have focused on the steady, inertialess flow regime. In this regime, by leveraging the FSIs, a myriad of applications to microfluidics have been proposed, such as: pressure sensors (Hosokawa et al., 2002; Ozsun et al., 2013), strain sensors (Dhong et al., 2018), micro-rheometers with increased sensitivity (Shiba et al., 2021), and passive technique for profiling microchannels’ shape (Karan et al., 2021). More recently, microfluidic systems have also begun to access inertial flow regimes up to a Reynolds number  $Re \simeq 10^2$  (Di Carlo et al., 2007). Although this range of  $Re$  is low compared to the well-documented flow-instability  $Re$  for flows in rigid conduits, flows in compliant micro-conduits, surprisingly, have been observed to go unstable. Dye stream experiments in a rectangular microchannel with a soft bottom wall by Verma and Kumaran (2013) showed that the stream begins to oscillates at  $Re \approx 178$  and can break up at  $Re \approx 200$ . Other experimental studies confirmed the existence of this phenomenon, in both channels and tubes (Krindel and Silberberg, 1979; Verma and Kumaran, 2012; Neelamegam and Shankar, 2015; Kumaran and Bandaru, 2016). Verma and Kumaran (2013) suggested that the instabilities observed are induced by FSIs. Importantly, the resulting unstable flows increased the mixing efficiency by several orders of magnitude, compared to a stable steady flow. This observation has important implications for new strategies of harnessing FSI-induced instabilities to enhance mixing at the microscale, which is notoriously challenging (Ottino and Wiggins, 2004; Karnik, 2013). Verma and Kumaran (2013) thus introduced the terms “ultrafast mixing” and “soft-wall turbulence” to refer these novel phenomena. However, it should be noted that FSI-induced unstable flows are fundamentally different from the usual wall-bounded turbulent flows at high  $Re$  (Srinivas and Kumaran, 2015, 2017).

Importantly, here, the low- $Re$  flows of interest are *not* such that  $Re \rightarrow 0$ . The flows of interest can be up to  $Re \simeq 10^2$ . Further, since the flow conduits in microfluidics are often manufactured to be long and slender, the “reduced”  $\hat{Re} = \epsilon Re$  is more suitable for quantifying the inertial effects in the flow, as we will show in section 3. Here,  $\epsilon$  is the aspect ratio of the conduit (radius to length for a tube, or height to length for a channel). We find that the observed instabilities in soft micro-conduits typically occur at  $\hat{Re}$  up to  $\mathcal{O}(1)$ . In this distinguished regime of  $\hat{Re}$ , the flow cannot be considered as inertialess or inviscid. Actually, there exists a balance between the fluid inertia and the dominant pressure gradient and viscous forces, as we will show in section 3.

However, even at low  $Re$ , analyzing the instability of pressure-driven flows in compliant conduits is far more challenging than that in rigid conduits. One key challenge is that, due to FSI, the base state is not the classical unidirectional flow solution for a rigid conduit (*e.g.*, the Poiseuille or Hagen–Poiseuille flows). At

	Flat base?	$\hat{Re} = \epsilon Re$	Instability type	Method
<b>Kumaran family</b>				
<a href="#">Kumaran (1995)</a>	Yes	$\mathcal{O}(1)$	Local	OS
<a href="#">Gkanis and Kumar (2005)</a>	No	$\mathcal{O}(1)$	Local	OS
<a href="#">Gaurav and Shankar (2009)</a>	Yes	$\mathcal{O}(1)$	Local	OS
<a href="#">Verma and Kumaran (2013)</a>	No	$\mathcal{O}(1)$	Local	OS
<a href="#">Verma and Kumaran (2015)</a>	No	$\mathcal{O}(1)$	Local	OS
<b>Collapsible tubes</b>				
<a href="#">Jensen (1990, 1992)</a>	No	$\gg 1$	Global	RM
<a href="#">Luo and Pedley (1996, 1998)</a>	No	$\gg 1$	Global	Num.
<a href="#">Jensen and Heil (2003)</a>	No	$\gg 1$	Global	Asym. & Num.
<a href="#">Luo et al. (2008)</a>	No	$\gg 1$	Global	Num.
<a href="#">Stewart et al. (2009)</a>	Yes	$\gg 1$	Global & Local	RM
<a href="#">Stewart et al. (2010)</a>	Yes	$\gg 1$	Global & Local	OS & MLEE
<a href="#">Heil and Boyle (2010)</a>	Yes	$\gg 1$	Global	Num.
<a href="#">Liu et al. (2012)</a>	No	$\gg 1$	Global	Num.
<a href="#">Xu et al. (2013, 2014)</a>	Yes	$\gg 1$	Global	RM
<a href="#">Pihler-Puzović and Pedley (2014)</a>	No	$\gg 1$	Global	RM
<a href="#">Wang et al. (2021)</a>	No	$\gg 1$	Global	Num.
<b>Present work</b>	No	$\mathcal{O}(1)$	Global	RM

Table 1: Comparison of selected previous studies on instability of pressure-driven flows in compliant conduits. In the last column, ‘OS’ stands for Orr–Sommerfeld-type stability analysis; ‘RM’ stands for reduced modeling; ‘Num.’ specifically stands for 2D two-way coupled FSI simulations; ‘Asym.’ stands for asymptotic analysis; and ‘MLEE’ stands for matched local eigenfunction expansion method.

steady state, a compliant channel will deform due to the hydrodynamic pressure within, and this deformation will, in turn, influence the velocity and pressure fields in the flow ([Gervais et al., 2006](#); [Christov, 2022](#)). Since the pressure decreases along the flow-wise direction in a pressure-driven flow, the deformation is not uniform, with larger deformation near the inlet and smaller deformation near the outlet. This non-flat shape of the deformed channel was indeed observed in the experiments by [Verma and Kumaran \(2013\)](#), however its two-way coupled nature to the flow was not captured in previous stability models. Importantly, the coupling between the flow and the solid deformation gives rise to a *non-constant* pressure gradient in the streamwise direction, leading to a *nonlinear* relationship between the flow rate and the pressure drop ([Gervais et al., 2006](#); [Seker et al., 2009](#); [Christov et al., 2018](#)). Only a global stability analysis can take this spatially varying non-flat base state into account. However, global analyses are difficult to perform for three-dimensional (3D) FSI problems. To this end, in the present work, we undertake reduced-order modeling.

Previous studies on instabilities due to microscale FSIs analyzed the problem from the local perspective. This line of research is termed as the “Kumaran family,” and a list of representative studies is compared/contrasted in table 1. The Kumaran family studies typically derive a modified Orr–Sommerfeld equation by perturbing the fluid–solid interface with infinitesimal disturbances. Early studies neglected the effect of FSIs on the base state completely by taking the base flow to be the unidirectional one in a rigid conduit ([Kumaran, 1995](#); [Gaurav and Shankar, 2009](#)). Recent work by [Verma and Kumaran \(2013, 2015\)](#) sought to improve the linear stability analyses by incorporating the effect of nonuniform deformation of the conduit wall. However, instead of being derived from the governing equations of two-way couple FSI problem, the deformed shape of the channel was imaged experimentally and then reconstructed for use in computational fluid dynamics (CFD) simulations. By assuming steady flow, the simulated velocity profile and the pressure distribution were taken as the base state and “imported” into the linear stability analysis. Nevertheless, to arrive at an Orr–Sommerfeld equation, [Verma and Kumaran \(2013, 2015\)](#) had to assume that the variation of the channel deformation along the streamwise direction is so slow that the flow is nearly parallel. Thus, long-wave perturbations cannot be considered, and the analysis is strictly local. Notably, the local unstable modes were predicted to arise at  $Re \lesssim 100$ , both in compliant channels ([Gkanis and](#)

Kumar, 2005; Verma and Kumaran, 2013) and in compliant tubes (Verma and Kumaran, 2015). However, it is difficult to reach a unified understanding from the current state of this literature because the explanation regarding the onset of instability is different for each situations. For instance, considering a neo-Hookean material as the compliant wall (instead of a linearly elastic model one) modifies the linear stability of the flow in a compliant tube (Gaurav and Shankar, 2009). Different formulations of the linear stability analysis can also lead to completely different conclusions (Patne and Shankar, 2019). The most recent advances and perspectives following this line of research are thoroughly reviewed by Kumaran (2021).

To fill these knowledge gaps, in this work, we analyze the global stability of microscale flows undergoing FSI. Specifically, we address the effect of the non-flat deformed base state, and we construct a reduced (global) model to make the analysis accessible. The idea of reduced modeling is inspired by the research program on the collapsible tube; representative prior work is compared/contrasted in table 1. Although collapsible tubes research focuses on inertial flows with  $\hat{Re} \gg 1$ , and is not concerned with flows at the microscale, this research program has demonstrated the power of reduced modeling. Compared to complex two-way-coupled unsteady FSI simulations, reduced mathematical models are better suited for exploring the (potentially large) parameter space of such FSI problems. Reduced models can also aid the mathematical analysis and thus promote the understanding of the instability mechanisms. Although early one-dimensional (1D) reduced models (Shapiro, 1977) incorporated *ad hoc* assumptions, such as an empirical tube law for deformation and an energy loss term for flow separation, these models surprisingly provided good qualitative agreement with experimental observations (Jensen and Pedley, 1989) and predicted the expected complex oscillations (Jensen, 1990, 1992). More recently, Pihler-Puzović and Pedley (2014) constructed a 1D model based on the so-called interactive boundary layer theory and predicted oscillations induced by wall inertia. Meanwhile, Stewart et al. (2009) invoked the long-wave approximation and built a 1D model to study the global and local instabilities in collapsible tubes. This model was then used extensively to investigate the effect of the pre-tension of the soft wall (Stewart et al., 2010), the effect of the length of the downstream rigid segment (Xu et al., 2013, 2014), and the model was also applied to understand retinal venous pulsation (Stewart and Foss, 2019).

Along these lines, in this work, we derive a 1D FSI model inspired, in several ways, by the 1D model of Stewart et al. (2009). However, instead of considering  $\hat{Re} \gg 1$ , we focus on  $\hat{Re}$  up to  $\mathcal{O}(1)$ , consistent with the microchannel experiments of Verma and Kumaran (2013). The new model admits a non-flat fluid–solid interface at steady state, resulting from the nonlinear pressure distribution within the channel. We conduct a global stability analysis to properly take this spatially-varying base state into account, complementary to the local stability analyses in the Kumaran family of studies. With the finite fluid inertia and non-flat base state accounted for, our 1D FSI model is the first reduced model that addresses the global stability of pressure-driven flow in a compliant microchannel.

To this end, this paper is organized as follows. We introduce the configuration of the microchannel in section 2. In section 3, we invoke the lubrication approximation to simplify the governing equations of the internal flow. Assuming linear elasticity, we extract the dominant mechanism in the wall deformation through a scaling argument, leveraging the slenderness of the wall (section 4.1). Then in section 4.2, the obtained displacement field is averaged over the spanwise direction ( $\hat{x}$ ), reducing the three-dimensional (3D) system (figure 1(a)) to a two-dimensional (2D) one (figure 1(b)). The ultimate solid model is 1D, obtained by introducing weak inertia and weak deformation-induced tension (section 4.3). In section 5, we couple the 1D solid model with the depth-averaged Navier–Stokes equations to achieve a reduced 1D FSI model relating the wall deformation to the flow rate and the pressure in the flow. We analyze the base state of the 1D FSI model in section 6. Then in section 7, we conduct a global linear stability analysis based on the nonuniform inflated base state, the results of which are validated against unsteady numerical simulations of the 1D FSI model (section 8.1). The dynamics of the 1D FSI model is also simulated by taking the undeformed state as the initial condition (section 8.2). Finally, in section 9, we conclude with a summary of the key results of our study, and their broader context.

## 2 Problem statement

Consider a microchannel, as shown in figure 1(a), with undeformed height of  $h_0$ , width of  $w$ , and length of  $\ell$ . The microchannel is assumed to be long and shallow so that  $h_0 \ll w \ll \ell$ . Introducing the dimensionless

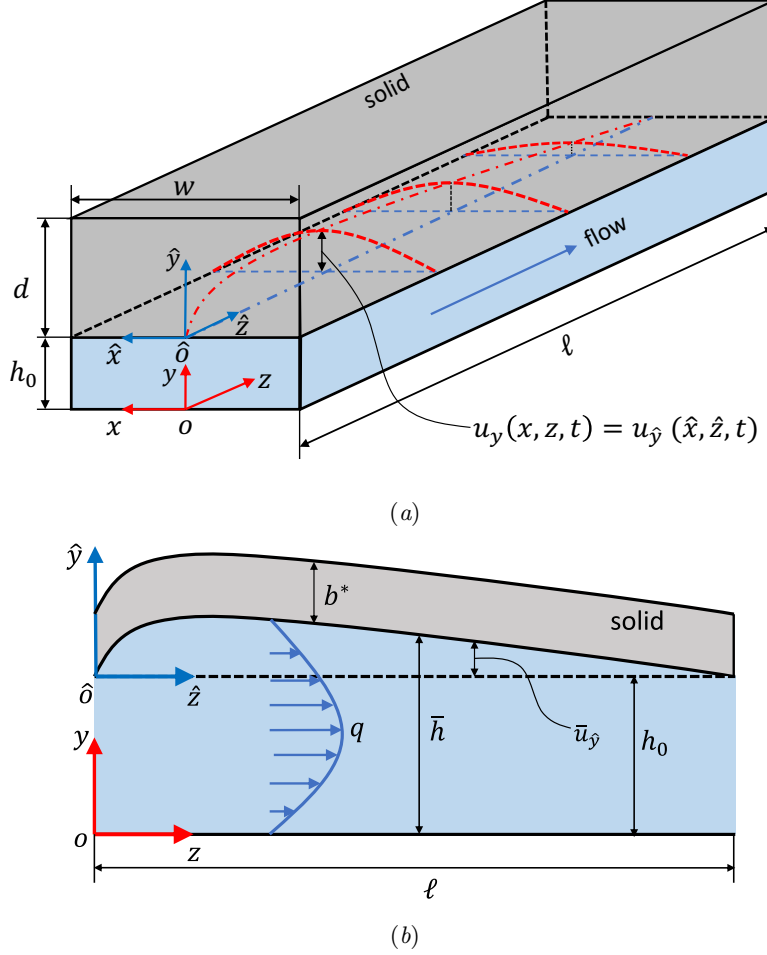


Figure 1: (a) Schematic of the 3D geometry of the compliant microchannel with a deformable top wall (Wang and Christov, 2021), with key dimensional variables labeled. The red dash-dotted curve and the red dashed curves sketch the deformed fluid–solid interface at the mid-plane ( $x = 0$ ), and the typical cross-sectional deformation profiles at the interface at different flow-wise locations, respectively. (b) Schematic of the configuration of the reduced 2D problem obtained by width-averaging the interface displacement.

parameters  $\epsilon = h_0/\ell$  and  $\delta = h_0/w$ , then we have  $\epsilon \ll \delta \ll 1$ . In reality, the three walls of the channel can be made rigid with a soft wall bonded on top, as the geometry considered in (Christov et al., 2018; Shidhore and Christov, 2018). Alternatively, the top and side walls are soft and bonded to rigid bottom wall, as was the case in (Wang and Christov, 2019). In either case, the deformation of the top wall is dominant. Therefore, in our modeling, the deformation of the side walls is neglected. Further, we denote the thickness of the top wall by  $d$ . To make the model general, at this stage, we do not specify the magnitude  $d$  compared to the other dimensions, but we do require that  $d \ll \ell$ . As the fluid is pushed through the microchannel, from the inlet to the outlet, the hydrodynamic pressure will deform the fluid–solid interface at the top wall. The displacement of the interface is denoted by  $u_y(x, z, t)$ . Finally, since the microchannel is often restricted from moving at the inlet ( $z = 0$ ) and the outlet ( $z = \ell$ ) planes by external connections (or the outlet is open to ambient gauge pressure, thus has negligible deformation), we assume zero displacement of the fluid–solid interface at both ends ( $z = 0, \ell$ ).

For convenience, we introduce two coordinate systems. As shown in figure 1(a), the  $o_{xyz}$  coordinate system is located at the bottom wall of the microchannel, with its origin set at the center of the inlet. The  $\hat{o}_{\hat{x}\hat{y}\hat{z}}$  coordinate system is the  $o_{xyz}$  system translated along  $y$  by  $h_0$ , thus its origin is located at the undeformed fluid–solid interface. Specifically, we have  $x = \hat{x}$ ,  $y = \hat{y} + h_0$  and  $z = \hat{z}$ .

Var.	$t$	$x$ or $\hat{x}$	$y$	$\hat{y}$	$z$ or $\hat{z}$	$v_x$	$v_y$	$v_z$	$p$
Scale	$\mathcal{T}_f$	$w$	$h_0$	$d$	$\ell$	$\epsilon\mathcal{V}_c/\delta$	$\epsilon\mathcal{V}_c$	$\mathcal{V}_c$	$\mathcal{P}_c$

Table 2: The scales for the variables in the incompressible Navier–Stokes equations (3.1).

### 3 Fluid mechanics problem formulation

#### 3.1 Scaling and identification of the dominant effects

Assume the working fluid is incompressible and Newtonian, with a density of  $\rho_f$  and dynamic viscosity of  $\mu$ . With the displacement of the fluid–solid interface denoted as  $u_y(x, z, t)$ , the deformed channel height can be written as  $h(x, z, t) = h_0 + u_y(x, z, t)$ . Then, the deformed configuration of the fluid domain is  $\{(x, y, z) \mid -w/2 \leq x \leq +w/2, 0 \leq y \leq h(x, z, t), 0 \leq z \leq \ell\}$ . Further, we assume that  $h(x, z, t) \ll w \ll \ell$ , *i.e.*, the slenderness and shallowness assumptions on the conduit hold true even after its deformation. The former assumption is important because it allows us to use  $h_0$  as the scale for  $y$ .

Under these assumptions, the governing equations are the unsteady incompressible Navier–Stokes equations, which take the form:

$$\underbrace{\frac{\partial v_x}{\partial x}}_{\mathcal{O}(1)} + \underbrace{\frac{\partial v_y}{\partial y}}_{\mathcal{O}(1)} + \underbrace{\frac{\partial v_z}{\partial z}}_{\mathcal{O}(1)} = 0, \quad (3.1a)$$

$$\underbrace{\frac{\partial v_x}{\partial t}}_{\mathcal{O}(\epsilon^2\delta^{-2}\hat{Re})} + \underbrace{v_x \frac{\partial v_x}{\partial x}}_{\mathcal{O}(\epsilon^2\delta^{-2}\hat{Re})} + \underbrace{v_y \frac{\partial v_x}{\partial y}}_{\mathcal{O}(\epsilon^2\delta^{-2}\hat{Re})} + \underbrace{v_z \frac{\partial v_x}{\partial z}}_{\mathcal{O}(\epsilon^2\delta^{-2}\hat{Re})} = -\underbrace{\frac{1}{\rho_f} \frac{\partial p}{\partial x}}_{\mathcal{O}(1)} + \underbrace{\frac{\mu}{\rho_f} \frac{\partial^2 v_x}{\partial x^2}}_{\mathcal{O}(\epsilon^2)} + \underbrace{\frac{\mu}{\rho_f} \frac{\partial^2 v_x}{\partial y^2}}_{\mathcal{O}(\epsilon^2\delta^{-2})} + \underbrace{\frac{\mu}{\rho_f} \frac{\partial^2 v_x}{\partial z^2}}_{\mathcal{O}(\epsilon^4\delta^{-2})}, \quad (3.1b)$$

$$\underbrace{\frac{\partial v_y}{\partial t}}_{\mathcal{O}(\epsilon^2\hat{Re})} + \underbrace{v_x \frac{\partial v_y}{\partial x}}_{\mathcal{O}(\epsilon^2\hat{Re})} + \underbrace{v_y \frac{\partial v_y}{\partial y}}_{\mathcal{O}(\epsilon^2\hat{Re})} + \underbrace{v_z \frac{\partial v_y}{\partial z}}_{\mathcal{O}(\epsilon^2\hat{Re})} = -\underbrace{\frac{1}{\rho_f} \frac{\partial p}{\partial y}}_{\mathcal{O}(1)} + \underbrace{\frac{\mu}{\rho_f} \frac{\partial^2 v_y}{\partial x^2}}_{\mathcal{O}(\epsilon^2\delta^2)} + \underbrace{\frac{\mu}{\rho_f} \frac{\partial^2 v_y}{\partial y^2}}_{\mathcal{O}(\epsilon^2)} + \underbrace{\frac{\mu}{\rho_f} \frac{\partial^2 v_y}{\partial z^2}}_{\mathcal{O}(\epsilon^4)}, \quad (3.1c)$$

$$\underbrace{\frac{\partial v_z}{\partial t}}_{\mathcal{O}(\hat{Re})} + \underbrace{v_x \frac{\partial v_z}{\partial x}}_{\mathcal{O}(\hat{Re})} + \underbrace{v_y \frac{\partial v_z}{\partial y}}_{\mathcal{O}(\hat{Re})} + \underbrace{v_z \frac{\partial v_z}{\partial z}}_{\mathcal{O}(\hat{Re})} = -\underbrace{\frac{1}{\rho_f} \frac{\partial p}{\partial z}}_{\mathcal{O}(1)} + \underbrace{\frac{\mu}{\rho_f} \frac{\partial^2 v_z}{\partial x^2}}_{\mathcal{O}(\delta^2)} + \underbrace{\frac{\mu}{\rho_f} \frac{\partial^2 v_z}{\partial y^2}}_{\mathcal{O}(1)} + \underbrace{\frac{\mu}{\rho_f} \frac{\partial^2 v_z}{\partial z^2}}_{\mathcal{O}(\epsilon^2)}, \quad (3.1d)$$

with the order-of-magnitude of each term listed underneath, based on the scales from table 2.

In table 2,  $\mathcal{V}_c$  is the characteristic velocity scale. Specifically, to ensure the conservation of mass of equation (3.1a),  $\epsilon\mathcal{V}_c/\delta$ ,  $\epsilon\mathcal{V}_c$  and  $\mathcal{V}_c$  are chosen to be the characteristic scales for the velocity components  $v_x$ ,  $v_y$  and  $v_z$ , respectively. Also, as is standard for low-Reynolds-number flow, to achieve a balance between the pressure and the viscous stresses in equation (3.1d), the characteristic pressure scale,  $\mathcal{P}_c$ , and  $\mathcal{V}_c$  are related by  $\mathcal{P}_c = \mu\mathcal{V}_c\ell/h_0^2$ . If the volumetric flow rate,  $q$ , at the inlet is fixed, we can choose  $\mathcal{V}_c = q/(wh_0)$ , then  $\mathcal{P}_c = \mu q\ell/(wh_0^3)$ . However, if the pressure drop,  $\Delta p = p|_{z=0} - p|_{z=\ell}$ , is prescribed,  $\mathcal{P}_c = \Delta p$  and, accordingly,  $\mathcal{V}_c = \Delta p h_0^2/(\mu\ell)$ . The Reynolds number is defined as  $Re = \rho_f\mathcal{V}_c h_0/\mu$ . However, the slenderness of the fluid domain makes the reduced Reynolds number,  $\hat{Re} = \epsilon Re$  more suitable for quantifying the inertial effects of the flow. Finally,  $\mathcal{T}_f$  is taken to be the characteristic time scale for axial advection (the dominant flow direction):  $\mathcal{T}_f = \ell/\mathcal{V}_c$ .

#### 3.2 Reduction: lubrication approximation

Recall that we are interested in the regime of  $\epsilon \ll \delta \ll 1$ . Based on the discussion above, it is clear that the dominant balance of terms occurs in the  $z$ -momentum equation (3.1d). Only the pressure terms are left in equations (3.1b) and (3.1c), indicating that, at the leading order in  $\epsilon$  and  $\delta$ , the hydrodynamic pressure  $p$  is *only* a function of the streamwise location  $z$ , as in the classic lubrication approximation (Panton, 2013; White, 2006). More importantly, this argument is true even at finite Reynolds number, *i.e.*,  $\hat{Re} = \mathcal{O}(1)$ , which is typical of the microfluidic experiments we compare to (Verma and Kumaran, 2013). Specifically,



Var.	$t$	$\hat{x}$	$\hat{y}$	$\hat{z}$	$u_{\hat{x}}$	$u_{\hat{y}}$ or $u_y$	$u_{\hat{z}}$	$\sigma_{\hat{x}\hat{x}}$	$\sigma_{\hat{x}\hat{y}}$	$\sigma_{\hat{x}\hat{z}}$	$\sigma_{\hat{y}\hat{y}}$	$\sigma_{\hat{y}\hat{z}}$	$\sigma_{\hat{z}\hat{z}}$
Scale	$\mathcal{T}_f$	$w$	$d$	$\ell$	$\mathcal{U}_{c,x}$	$\mathcal{U}_c$	$\mathcal{U}_{c,z}$	$\mathcal{D}_{\hat{x}\hat{x}}$	$\mathcal{D}_{\hat{x}\hat{y}}$	$\mathcal{D}_{\hat{x}\hat{z}}$	$\mathcal{P}_c$	$\epsilon\mathcal{P}_c$	$\mathcal{D}_{\hat{z}\hat{z}}$

Table 3: The scales for the variables in the linear elastodynamics equations (4.1).

with  $\hat{R}e = \mathcal{O}(1)$ , the dominant balance in the flow-wise momentum equation (3.1d) occurs between fluid inertia, the pressure gradient, and the viscous forces. The same balance was employed by Inamdar et al. (2020) to derive a 1D FSI model from the 2D Navies–Stokes equations (but under different assumptions on the solid mechanics problem).

Examining further the right-hand side of equation (3.1d), the balance of forces at the leading-order indicates that  $\partial p/\partial z \sim \partial \tau_{yz}/\partial y$  because the shear stress is  $\tau_{yz} \sim \mu \partial v_z/\partial y$ . Introducing  $\mathcal{S}_c$  as the characteristic scale for  $\tau_{yz}$  and substituting the other scales from table 2, the balance suggests that  $\mathcal{P}_c/\ell = \mathcal{S}_c/h_0$ , leading to  $\mathcal{S}_c = h_0/\ell \mathcal{P}_c = \epsilon \mathcal{P}_c$ . For  $\epsilon \ll 1$ , we conclude that  $\tau_{yz} \ll p$ . Hence, at the leading order in  $\epsilon$  and  $\delta$ ,  $p(z)$  is the only flow-induced load exerted on the fluid–solid interface.

## 4 Solid mechanics problem formulation

### 4.1 Scaling and identification of the dominant effects

For solid mechanics problem, it is more convenient to use the  $\hat{x}\hat{y}\hat{z}$  coordinate system, where we denote the displacement of the fluid–solid interface by  $u_{\hat{y}}$ , as shown in figure 1(a). We consider the case in which the maximum of  $u_{\hat{y}}$  is small compared with the smallest dimension of the solid, so that the small-strain theory of linear elasticity is applicable. Specifically, if the wall is “thick,” meaning  $w \lesssim d \ll \ell$ , we require that  $u_{\hat{y}} \ll w$ . However, if the wall is “thin,” meaning  $d \lesssim w \ll \ell$ , we require that  $u_{\hat{y}} \ll d$  (Wang and Christov, 2021).

The following discussion follows that of Wang and Christov (2019). However, here, we provide a more general derivation for the reader’s convenience. First, using the scales from table 3, the balance between the Cauchy stresses and the solid inertia within the wall, neglecting any body forces,

$$\underbrace{\rho_s \frac{\partial^2 u_{\hat{x}}}{\partial t^2}}_{\mathcal{O}(\rho_s \mathcal{U}_{c,x}/\mathcal{T}_f^2)} + \underbrace{\frac{\partial \sigma_{\hat{x}\hat{x}}}{\partial \hat{x}}}_{\mathcal{O}(\mathcal{D}_{\hat{x}\hat{x}}/w)} + \underbrace{\frac{\partial \sigma_{\hat{x}\hat{y}}}{\partial \hat{y}}}_{\mathcal{O}(\mathcal{D}_{\hat{x}\hat{y}}/d)} + \underbrace{\frac{\partial \sigma_{\hat{x}\hat{z}}}{\partial \hat{z}}}_{\mathcal{O}(\mathcal{D}_{\hat{x}\hat{z}}/\ell)} = 0, \quad (4.1a)$$

$$\underbrace{\rho_s \frac{\partial^2 u_{\hat{y}}}{\partial t^2}}_{\mathcal{O}(\rho_s \mathcal{U}_c/\mathcal{T}_f^2)} + \underbrace{\frac{\partial \sigma_{\hat{x}\hat{y}}}{\partial \hat{x}}}_{\mathcal{O}(\mathcal{D}_{\hat{x}\hat{y}}/w)} + \underbrace{\frac{\partial \sigma_{\hat{y}\hat{y}}}{\partial \hat{y}}}_{\mathcal{O}(\mathcal{P}_c/d)} + \underbrace{\frac{\partial \sigma_{\hat{y}\hat{z}}}{\partial \hat{z}}}_{\mathcal{O}(\epsilon \mathcal{P}_c/\ell)} = 0, \quad (4.1b)$$

$$\underbrace{\rho_s \frac{\partial^2 u_{\hat{z}}}{\partial t^2}}_{\mathcal{O}(\rho_s \mathcal{U}_{c,z}/\mathcal{T}_f^2)} + \underbrace{\frac{\partial \sigma_{\hat{x}\hat{z}}}{\partial \hat{x}}}_{\mathcal{O}(\mathcal{D}_{\hat{x}\hat{z}}/w)} + \underbrace{\frac{\partial \sigma_{\hat{y}\hat{z}}}{\partial \hat{y}}}_{\mathcal{O}(\epsilon \mathcal{P}_c/d)} + \underbrace{\frac{\partial \sigma_{\hat{z}\hat{z}}}{\partial \hat{z}}}_{\mathcal{O}(\mathcal{D}_{\hat{z}\hat{z}}/\ell)} = 0. \quad (4.1c)$$

Here,  $\sigma_{\hat{x}\hat{x}}$ ,  $\sigma_{\hat{x}\hat{y}}$ ,  $\sigma_{\hat{x}\hat{z}}$ ,  $\sigma_{\hat{y}\hat{y}}$ ,  $\sigma_{\hat{y}\hat{z}}$  and  $\sigma_{\hat{z}\hat{z}}$  are the six independent components of the Cauchy stress in the solid. The order-of-magnitude of each term is listed underneath, based on the scales from table 3.

In table 3,  $\mathcal{U}_{c,x}$ ,  $\mathcal{U}_c$  and  $\mathcal{U}_{c,z}$  are the characteristic scales for  $u_{\hat{x}}$ ,  $u_{\hat{y}}$  and  $u_{\hat{z}}$ , respectively. We immediately assume that  $\mathcal{U}_{c,x} \ll \mathcal{U}_c$  and  $\mathcal{U}_{c,z} \ll \mathcal{U}_c$ , meaning that the wall is primarily bulging upwards, as in experiments. This assumption has previously been quantitatively validated against experiments (Christov et al., 2018; Shidhore and Christov, 2018; Wang and Christov, 2019). Then the most prominent inertial term in the solid is in equation (4.1b). Note that the time scale for equation (4.1) is still the fluid’s axial advection time scale,  $\mathcal{T}_f$ , in order to ensure the coupling between the solid and the fluid mechanics problems. (Note that this choice of time scale is different from the so-called “viscous–elastic” one used in related works (Elbaz and Gat, 2014; Martínez-Calvo et al., 2020). In the latter papers, the characteristic (common) time scale  $\mathcal{T}_c$  was chosen based on the kinematic boundary condition at the fluid–solid interface, *i.e.*,  $\partial \bar{u}_y/\partial t = v_y$ , leading to a fluid time scale of  $\mathcal{T}_c = \bar{\mathcal{U}}_c/(\epsilon \mathcal{V}_c) = (\bar{\mathcal{U}}_c/h_0)(\ell/\mathcal{V}_c) = \beta \mathcal{T}_f$ . However, since  $\beta$  is typically at  $\mathcal{O}(1)$  in our work (discussed in section 4.4), these two different choices of the fluid time scale,  $\mathcal{T}_c$  and  $\mathcal{T}_f$ , do not differ

significantly.) To further elucidate the time scales involved, the scaling of the inertial term in equation (4.1b) can be written as  $\rho_s \mathcal{U}_c / \mathcal{T}_s^2 \times (\mathcal{T}_s / \mathcal{T}_f)^2$ , where we have explicitly introduced the solid time scale,  $\mathcal{T}_s$ . As we will show in section 4.3.1, in the microfluidic setting,  $\mathcal{T}_s \ll \mathcal{T}_f$ , leading to  $\rho_s \mathcal{U}_c / \mathcal{T}_f^2 \ll 1$ , thus the inertia of the solid is a weak effect.

Next, let us consider the balance of the Cauchy stresses. Due to the traction balance at the fluid–solid interface, it can be inferred that  $\mathcal{D}_{\hat{y}\hat{y}} = \mathcal{P}_c$  and  $\mathcal{D}_{\hat{y}\hat{z}} = \epsilon \mathcal{P}_c$ , as tabulated in table 3. For convenience, we introduce  $\gamma = d/w$ . Then, a balance in equation (4.1b) can only occur between the second and the third terms, yielding  $\mathcal{D}_{\hat{x}\hat{y}} = \mathcal{P}_c / \gamma$ . At the same time, the balance of the three terms in equation (4.1c) gives  $\mathcal{D}_{\hat{x}\hat{z}} = \epsilon \mathcal{P}_c w / d = \epsilon \mathcal{P}_c / \gamma$  and  $\mathcal{D}_{\hat{z}\hat{z}} = \epsilon \mathcal{P}_c \ell / d = \delta \mathcal{P}_c / \gamma$ . Finally, from equation (4.1a), the only remaining possibility is that the second term balances the third term, indicating  $\mathcal{D}_{\hat{x}\hat{x}} = w \mathcal{D}_{\hat{x}\hat{y}} / d = \mathcal{P}_c / \gamma^2$ .

So far, we have only required that  $d \ll \ell$ , which is equivalent to  $\gamma \ll \delta / \epsilon$ , and covers a large range of wall thicknesses. However, it is also expected that  $\gamma \gg \epsilon$ , such that  $\mathcal{D}_{\hat{x}\hat{z}}$  is a small quantity, excluding the case of an extremely thin wall. In fact, recalling that the application of linear elasticity requires that  $\hat{u}_y \ll d$ , any prominent deformation in a thin-walled microchannel is likely out of the scope of the linear elastic theory.

Therefore, with  $\epsilon \ll \gamma \ll \delta / \epsilon$  as well as  $\epsilon \ll \delta \ll 1$ , it is concluded that  $\sigma_{\hat{x}\hat{z}}$  and  $\sigma_{\hat{y}\hat{z}}$  are negligible compared to the other components. Depending on the wall thickness, the relative magnitude among the remaining four stress components can change. For example, if  $\gamma^2 \gg 1$ , we can further neglect  $\sigma_{\hat{x}\hat{x}}$  as in (Wang and Christov, 2019). Nevertheless, no matter how  $d$  varies, the dominant balances in equations (4.1a) and (4.1b) occur in the cross-sectional  $(\hat{x}, \hat{y})$  plane, which reduces the original 3D elasticity problem to a 2D plane-strain problem. Since it has been shown in section 3 that  $p$  is a function of  $z$  only at the leading order (in  $\epsilon$ ), the deformation of the  $(\hat{x}, \hat{y})$  cross-sections at different  $z$ -locations (recalling  $z = \hat{z}$ ) decouple from each other. At each cross-section, the deformation is then determined by the local hydrodynamic pressure  $p(z, t)$ . Therefore, generally, we can express the displacement of the fluid–solid interface at the leading order (in  $\epsilon$ ) as

$$u_y(x, z, t) = u_{\hat{y}}(\hat{x}, \hat{z}, t) = \mathbf{f}(x)p(z, t), \quad (4.2)$$

with  $\mathbf{f}(x)$  being the spanwise deformation profile. The separation-of-variables form of equation (4.2) suggests that the cross-sectional deformation profiles at different  $z$ -locations are, in a sense, self-similar. The displacement is fully determined by the local pressure, showing that the fluid–solid interface behaves like a Winkler foundation (Winkler, 1867; Dillard et al., 2018), with a variable stiffness represented by  $1/\mathbf{f}(x)$ . Importantly, this Winkler-foundation-like mechanism is *not* an assumption here, but rather it is a *consequence* of the slenderness of the top wall. Also, note that the assumption of  $\mathcal{T}_s \ll \mathcal{T}_f$  has been applied here, meaning that the solid responds to pressure changes in the flow promptly.

It is also worth mentioning that if the top wall is thin with  $\epsilon \ll \gamma \lesssim 1$ , the elasticity problem is usually taken to be a plane stress problem, and a 1D engineering model is usually available for the displacement out of plane (*i.e.*,  $u_y$  here), such as the Kirchhoff–Love (Love, 1888; Timoshenko and Woinowsky-Krieger, 1959) and Reissner–Mindlin (Reissner, 1945; Mindlin, 1951) plate theories. However, this fact does not fundamentally contradict with our plane-strain reduction because the decoupling of the cross-sections remains true (Christov et al., 2018; Shidhore and Christov, 2018; Anand et al., 2020) due to the separation of scales,  $w \ll \ell$ .

Moreover, the discussion above is only based on the balance of Cauchy stresses, and does not involve the boundary conditions either on the sides (*i.e.*, at  $x = \pm w/2$ ) or at the upper surface of the wall (*i.e.*, at  $\hat{y} = d$  or  $y = h_0 + d$ ). The decoupling of the cross-sectional deformation is just a consequence of the wall slenderness. However, the boundary conditions do have an important influence on the displacement field in the solid, which will give rise to different forms of  $\mathbf{f}(x)$  in equation (4.2) (Wang and Christov, 2021).

## 4.2 Reduction: introducing the width-averaged (effective) height

Since we seek a 1D model dependent on  $z$  only, the  $x$ -dependence can be eliminated by averaging the displacement of the fluid–solid interface over  $x$ :

$$\bar{u}_y(z, t) = \frac{1}{w} \int_{-w/2}^{+w/2} u_y(x, z, t) dx = \underbrace{\left[ \frac{1}{w} \int_{-w/2}^{+w/2} \mathbf{f}(x) dx \right]}_{1/k} p(z, t), \quad (4.3)$$



having used equation (4.2). Then, the width-averaged height  $\bar{h}$  of the channel is

$$\bar{h}(z, t) = \frac{1}{w} \int_{-w/2}^{+w/2} h_0 + u_y(x, z, t) dx = h_0 + \frac{1}{k} p(z, t). \quad (4.4)$$

An important quantity in the above equations is the proportionality constant,  $k$ , which represents the *effective stiffness* of the interface and further reinforces the Winkler-foundation-like mechanism of deformation of the fluid–solid interface.

Equation (4.4) simplifies the FSI problem in two aspects. First, the deformation of the interface is further reduced from 2D to 1D. Second, the flow in the channel is reduced from 3D to 2D, and this reduction does not change any key statements made before. In other words, if we start from the 2D incompressible Navier–Stokes equations (simply neglecting  $v_x$  and  $x$ -dependent terms), we still find the lubrication approximation is applicable up to  $\hat{Re} = \mathcal{O}(1)$ , as in section 3.2.

In the following discussion, we will take  $\bar{h}$  as the effective height of the deformed channel and consider the reduced system sketched in figure 1(b). Taking  $\bar{h}$  as the effective deformed height was first put forward by Gervais et al. (2006). As shown by Wang and Christov (2021), the error introduced by this averaging approach is controllable.

### 4.3 Extension: introducing weak deformation effects

So far, the discussion in the previous subsections was based on the leading-order (in  $\epsilon$ ) theory, which does not take into account the possible restrictions imposed at the inlet and the outlet (*i.e.*, at  $z = 0$  and  $z = \ell$ ). As shown in figure 1(b), the movement of the fluid–solid interface at both ends is often physically restricted. In this sense, we can think of the solid mechanics problem as being essentially a boundary layer problem. While the Winkler-foundation-like mechanism is dominant outside the “boundary layers” near the inlet and outlet, with equation (4.3) being the (outer) solution there, another mechanism plays a role within thin (boundary) layers near  $z = 0, \ell$ , each admitting inner solutions that regularize the problem and allow the enforcement of end constraints.

Since the bulging of the top wall unavoidably introduces stretching along  $z$  in the solid, a simple extension of equation (4.3) can be achieved by introducing weak constant tension into the formulation (Wang and Christov, 2021). First, for the Winkler-foundation-like mechanism to be dominant, the tension needs to be “weak.” Second, the tension force can be taken to be constant because its variation along  $z$  is proportional to the fluid’s tangential traction at the interface, which is a small quantity per the lubrication approximation, as shown in section 3 (see also Hewitt et al., 2015). The “regularized” governing equations for  $\bar{u}_y$  is then written as

$$\rho_s b^* \frac{\partial^2 \bar{u}_y}{\partial t^2} + k \bar{u}_y - \chi_t \frac{\partial^2 \bar{u}_y}{\partial z^2} = p(z, t), \quad (4.5)$$

where  $\rho_s$  denotes the solid density,  $b^*$  represents the effective thickness of the interface (discussed in section 4.3.1), and  $\chi_t$  is the tension per unit width (discussed in section 4.3.2), respectively. Also recall that  $k$  is the effective stiffness introduced in equation (4.3). The weakness of the solid inertia and the tension is not obvious from equation (4.5), but will become clear after we introduce the dimensionless variables.

Equation (4.5) is essentially the equation of motion of a Kramer-type surface, which has been used extensively in the study of high- $Re$  (boundary layer) flows over compliant coatings. The goal of the latter studies is to understand how to delay the laminar-turbulence transition (Gad-el Hak, 2002). However, microchannel flows cannot reach such high  $Re$  values. More surprisingly, the application of equation (4.5) in modeling soft microchannels leads to a different conclusions from the compliant coating studies. Compliance of the wall can actually promote (instead of delay) the laminar-turbulence transition thanks to the FSI-induced instabilities. This effect can be successfully exploited for micromixing.

#### 4.3.1 Effective interface thickness

The goal of previous studies was to find a solution for the fluid–solid interface displacement,  $\bar{u}_y$ , from which to determine the cross-sectional area of the deformed fluidic channel. To illustrate this point, consider the microchannel studied by Wang and Christov (2019), which has a similar configuration to figure 1(a). In this case, the theory of the flow-induced deformation predicts that the vertical displacement of the solid,

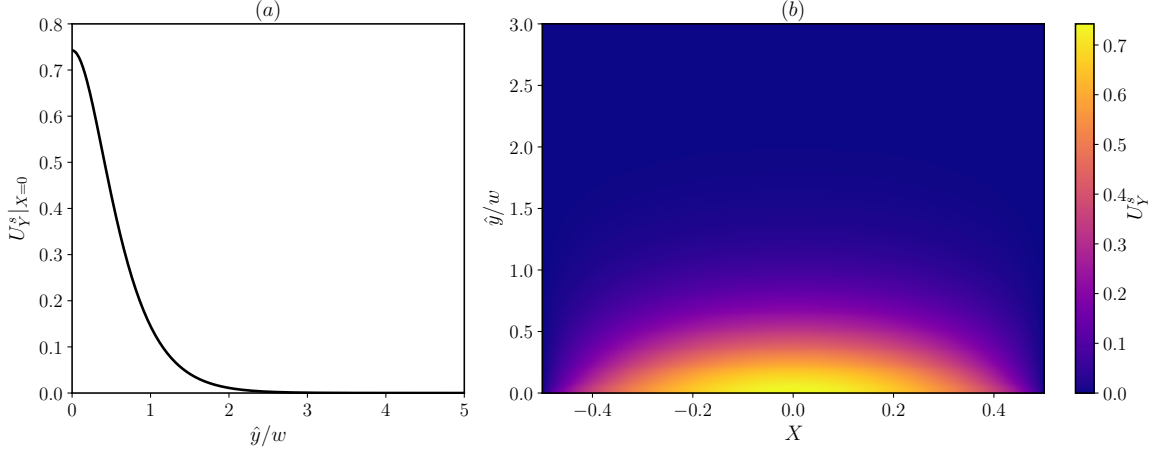


Figure 2: Illustration of the displacement field in a thick wall predicted by equation (3.14) from Wang and Christov (2019). (a) Centerline displacement at  $x/w = X = 0$  versus dimensionless vertical distance from the fluid–solid interface,  $\hat{y}/w$ . (b) Contour plot of the displacement field. Here,  $\hat{y} = y + h_0$  and  $\mathcal{U}_c = w\mathcal{P}_c/(h_0\bar{E})$ .

$U_Y^s = u_y^s(x, \hat{y}, z)/\mathcal{U}_c$ , varies with the vertical distance from the fluid–solid interface ( $\hat{y} = 0$ ), as shown in figure 2. For the unsteady in this work, however, we must properly connect the motion of the fluid–solid interface to the non-uniform motion of the entire top wall. Since this variation is rapidly decaying, it is reasonable to expect that a suitable *effective thickness* of the fluid–solid interface,  $b^*$ , can be introduced and used in equation (4.5). In doing so, the unsteady motion of the *whole* solid (of nonuniform vertical displacements) will be captured by the vertical motion of an *interface* of “virtual” thickness  $b^*$ .

In analogy to the definition of boundary layer thickness (Panton, 2013; White, 2006), we define  $b^*$  by requiring that the momentum of the solid wall’s motion is equivalent to the momentum of the reduced interface’s motion, *i.e.*,

$$\rho_s \int_0^d \int_{-w/2}^{+w/2} \dot{u}_y^s(x, \hat{y}, z) dx d\hat{y} = \rho_s w b^* \dot{\bar{u}}_y(z). \quad (4.6)$$

Since we have assumed that the solid deformation is governed by linear elasticity, the domain of integration is unchanged after deformation. Then, we can take the time derivative out of the integral. Substituting the definition of  $\bar{u}_y$ , we obtain

$$b^* = \frac{\int_0^d \int_{-w/2}^{+w/2} u_y^s(x, \hat{y}, z) dx d\hat{y}}{w \bar{u}_y} = \frac{\int_0^d \int_{-w/2}^{+w/2} u_y^s(x, \hat{y}, z) dx d\hat{y}}{\int_{-w/2}^{+w/2} u_y^s(x, 0, z) dx}. \quad (4.7)$$

Substituting equation (3.14) from Wang and Christov (2019) into equation (4.7), we find that  $b^* \approx 0.6141w$  for thick-walled microchannel ( $d^2/w^2 \gg 1$ ). However, if the top wall is thin ( $d \simeq w$ ), plate theory can be invoked, and the mid-plane displacement can represent the bulk motion of the interface; in this case,  $b^* = d$ .

#### 4.3.2 Weak tension

Having introduced  $b^*$ , we are ready to give an expression for the weak tension,  $\chi_t$ . One possible scenario is that  $\chi_t$  arises from the bulging of the wall. In principle, the deformation-induced tension is nonuniform along  $z$ . However, as mentioned, the variation of tension in  $z$  is balanced with the shear stress in the flow, and thus can be neglected. Then, assuming the in-plane displacement (along  $z$ ) is negligible,  $\chi_t$  can be estimated by the average stretch of the wall (Hewitt et al., 2015), written as

$$\chi_t = \frac{Eb^*}{\ell} \int_0^\ell \frac{1}{2} \left( \frac{\partial \bar{u}_y}{\partial z} \right)^2 dz. \quad (4.8)$$

Deformation-induced tension is expected to occur when the outlet of the channel is open to air, as in (Gervais et al., 2006; Verma and Kumaran, 2013), or the pre-tension provided by external connectors is negligible. In the unsteady case,  $\chi_t$  is time-dependent.

Another possible situation is that the microchannel is pre-stretched and installed between an upstream and downstream section, as in the research on collapsible tubes mentioned in section 1. With the increase of the flow rate, the bulging of the wall is more prominent, leading to larger  $\chi_t$ . However, beyond a certain flow rate, the deformation-induced tension will not be sufficient to hold the channel at the inlet and the outlet. In other words, the boundary conditions cannot be satisfied. The upper bound on the flow rate before the model breaks down is related to and found to increase with  $\chi_t$  (Wang and Christov, 2021). Therefore, in this case when the deformation-induced tension is not sufficient, if the system is still to operate at such a high flow rate, external pre-tension needs to be provided. Nevertheless, for the validity of equation (4.5), the pre-tension in this case should be much larger than the deformation-induced tension. On the other hand, the third term in equation (4.5) needs to be small compared with the second term, to ensure the dominance of the Winkler-foundation-like mechanism.

Apart from weak tension, other elastic forces might also be relevant. For example, if the top wall is thin, bending could play a role. Another example comes from the elastic structures on top of thin fluid films, wherein (in addition to tension) bending and gravity are invoked to regularize the problem (Peng and Lister, 2020). However, in the present work, we consider only the weak tension effect.

#### 4.4 Nondimensionalization: introducing the FSI parameter

We can now make the 1D interface motion equation (4.5) dimensionless to better illustrate the relative magnitude of the different terms (effects). Capital letters are used to denote the dimensionless variables.

The first step is to determine the characteristic scale,  $\bar{U}_c$ , for the fluid–solid interface. The dominant deformation effect in equation (4.3), suggests that we should take  $\bar{U}_c = \mathcal{P}_c/k$ , recalling that the scale for  $p$  is  $\mathcal{P}_c$ . Then, the dimensionless version of equation (4.3) is simply

$$\bar{U}_Y(Z, T) = P(Z, T). \quad (4.9)$$

Still using  $h_0$  to scale  $\bar{h}$ , the dimensionless effective channel height (equation (4.4)) becomes

$$\bar{H}(Z, T) = 1 + \frac{\bar{U}_c}{h_0} \bar{U}_Y(Z, T) = 1 + \beta \bar{U}_Y(Z, T). \quad (4.10)$$

Here, we have introduced another dimensionless parameter,  $\beta = \bar{U}_c/h_0 = \mathcal{P}_c/(kh_0)$ . It is clear from equation (4.10) that  $\beta$  translates the interface displacement into the deformation of the fluid domain, capturing the “strength” of the fluid–solid coupling. Thus,  $\beta$  is the “FSI parameter” of our model.

The dependence on  $\beta$  on the system properties comes through  $\mathcal{P}_c$  and  $k$ . While  $\mathcal{P}_c$  is determined by the flow conditions (*i.e.*, the viscosity of the fluid, the flow rate, and the geometry of the undeformed channel),  $k$  is determined by the material properties, the geometry, and the boundary conditions on the compliant wall. To explicitly show this, we write

$$\frac{1}{k} = \frac{1}{w} \int_{-w/2}^{+w/2} \mathfrak{f}(x) dx = \int_{-1/2}^{+1/2} \mathfrak{f}(wX) dX = \underbrace{\frac{\xi}{E} \int_{-1/2}^{+1/2} F(X) dX}_{\mathcal{I}_1} = \frac{\xi \mathcal{I}_1}{E}. \quad (4.11)$$

The definition of  $k$  from equation (4.3) is used in the first step. The second step is making the integral dimensionless. In the third step, the assumption of a linearly elastic solid has been invoked with  $k \propto \bar{E}$  and  $\mathfrak{f}(x) \propto 1/\bar{E}$ . Here,  $\bar{E} = E/(1 - \nu_s^2)$ , is used because of the plain-strain reduction, with  $E$  being the Young’s modulus and  $\nu_s$  being the Poisson’s ratio, respectively. Then,  $F(X)$  is introduced as the dimensionless self-similar deformation profile, and  $\xi$  is the resulting pre-factor after  $x$  is scaled by  $w$ . In the last step,  $\mathcal{I}_1 = \int_{-1/2}^{+1/2} F(X) dX$  was introduced to simplify the expression. While the effect of the material properties of the solid wall are captured by  $\bar{E}$ , the influence of the wall geometry and the boundary conditions are taken by both  $\xi$  and  $\mathcal{I}_1$ . As mentioned in section 4.1,  $\mathfrak{f}(x)$  takes different forms in different situations, thus giving different expressions of  $\xi$  and  $\mathcal{I}_1$ . For example, for the thick-walled microchannel considered by Wang

and Christov (2019),  $\xi = w$  and  $\mathcal{I}_1 \approx 0.542754$ . Meanwhile, for the microchannels with thick-plate-like top walls considered by Shidhore and Christov (2018),  $\xi = w^4/(2d^3)$  and  $\mathcal{I}_1 = \frac{1}{30} + \frac{(d/w)^2}{3\kappa(1-\nu_s)}$ , with  $\kappa$  (typically,  $\kappa = 1$ ) being a “shear correction factor.” Nevertheless, the key point is that both  $\xi$  and  $\mathcal{I}_1$  can be obtained *a priori*, by solving the corresponding elasticity problem, as analytical expressions.

Substituting the other scales from tables 2 and 3, the dimensionless version of equation (4.5) is

$$\theta_I \frac{\partial^2 \bar{U}_Y}{\partial T^2} + \bar{U}_Y - \theta_t \frac{\partial^2 \bar{U}_Y}{\partial Z^2} = P, \quad (4.12)$$

where  $\theta_I = \rho_s b^* \bar{U}_c / (\mathcal{T}_f^2 \mathcal{P}_c)$  and  $\theta_t = \chi_t \bar{U}_c / (\ell^2 \mathcal{P}_c)$  are introduced above as the inertial coefficient and the tension coefficient, respectively. As discussed in section (4.3),  $\theta_I \ll 1$  and  $\theta_t \ll 1$  is expected because both the solid inertia and the tension effect are weak. Then, as expected, the leading-order solution (as  $\theta_I, \theta_t \rightarrow 0$ ) of equation (4.12) is equation (4.9).

Let’s justify  $\theta_I \ll 1$  first. Recalling that  $\mathcal{P}_c = \mu \mathcal{V}_c / (\epsilon h_0)$ ,  $\hat{R}e = \epsilon \rho_f \mathcal{V}_c h_0 / \mu$ , and  $\beta = \bar{U}_c / h_0$ ,  $\theta_I$  can be written as

$$\theta_I = \frac{\rho_s b^* \bar{U}_c}{\mathcal{T}_f^2 \mathcal{P}_c} = \epsilon \frac{\rho_f \mathcal{V}_c h_0}{\mu} \frac{\bar{U}_c}{h_0} \frac{b^* h_0}{\ell^2} \frac{\rho_s}{\rho_f} = \epsilon \hat{R}e \beta \frac{b^*}{\ell} \frac{\rho_s}{\rho_f}. \quad (4.13)$$

Since  $\epsilon \ll 1$ ,  $b^* \leq d \ll \ell$ ,  $\hat{R}e = \mathcal{O}(1)$ ,  $\beta$  is typically  $\mathcal{O}(1)$  and  $\rho_s \simeq \rho_f$  in the microchannel setting (because PDMS has a similar density to water), we have justified  $\theta_I \ll 1$ . Note time in equation (4.5) is scaled by  $\mathcal{T}_f$ , as before, to ensure the fluid–solid coupling. The limit  $\theta_I \ll 1$  corresponds to  $\mathcal{T}_s^2 \ll \mathcal{T}_f^2$ , meaning that the solid does respond to the pressure change in the flow promptly. It is also helpful to note that, using equation (4.11), we can also write

$$\theta_I = \mathcal{I}_1 \frac{\rho_s b^* \xi}{\mathcal{T}_f^2 \bar{E}}, \quad (4.14)$$

which indicates that, for a more rigid solid (*i.e.*, with the increase of  $\bar{E}$ ), the solid deformation develops much faster than the flow.

Again using equation (4.11), the dimensionless tension coefficient can be written as

$$\theta_t = \frac{\chi_t \bar{U}_c}{\ell^2 \mathcal{P}_c} = \mathcal{I}_1 \frac{\chi_t \xi}{\bar{E} \ell^2}. \quad (4.15)$$

If  $\chi_t$  is deformation-induced (thus time-dependent), substituting equation (4.8) into equation (4.15), we obtain

$$\theta_t(T) = \mathcal{I}_1 \frac{\xi}{\bar{E} \ell^2} \frac{E b^*}{\ell} \int_0^\ell \frac{1}{2} \left( \frac{\partial \bar{u}_y}{\partial z} \right)^2 dz = (1 - \nu_s^2) \mathcal{I}_1 \frac{\xi b^* \bar{U}_c^2}{\ell^4} \int_0^1 \frac{1}{2} \left( \frac{\partial \bar{U}_Y}{\partial Z} \right)^2 dZ = \tilde{\theta}_t \int_0^1 \frac{1}{2} \left( \frac{\partial \bar{H}}{\partial Z} \right)^2 dZ, \quad (4.16)$$

where

$$\tilde{\theta}_t = \frac{1}{\beta^2} \times (1 - \nu_s^2) \mathcal{I}_1 \frac{\xi b^* \bar{U}_c^2}{\ell^4} = (1 - \nu_s^2) \mathcal{I}_1 \epsilon^2 \frac{\xi b^*}{\ell^2}. \quad (4.17)$$

Note that we have used equation (4.10) in the last step of the manipulations in equation (4.16). Also, note that  $\tilde{\theta}_t$  is not related to the flow conditions, and  $\tilde{\theta}_t \ll 1$  for microchannels. Within linear elasticity, the integral in equation (4.16) is  $\mathcal{O}(1)$ , thus  $\theta_t \ll 1$ .

Finally, the key dimensional and dimensionless parameters are summarized in table 4. Typical values for microfluidic systems are given to justify the bigness/smallness assumptions made.

## 5 Fluid–solid coupling: A new 1D FSI model

The final step in deriving the 1D FSI model involves coupling the fluid mechanics problem to the solid mechanics problem. This coupling is achieved by depth averaging the Navier–Stokes equations at the leading order in  $\epsilon$ . Recall that, even though we averaged across  $X$  in section 4.2, the flow field is 2D at this stage, *i.e.*,  $V_Z = V_Z^{2D}(Y, Z, T)$ . Vertically integrating the axial velocity,  $V_Z^{2D}$ , introduces the flow rate,

Quantity	Notation	Typical value	Units
channel's length	$\ell$	1.0	cm
channel's undeformed height	$h_0$	30	$\mu\text{m}$
channel's width	$w$	500	$\mu\text{m}$
top wall's thickness	$t$	2.0	mm
solid's Young's modulus	$E$	See table 5	MPa
solid's Poisson's ratio	$\nu$	0.5	–
solid's density	$\rho_s$	$1.0 \times 10^3$	$\text{kg m}^{-3}$
fluid's density	$\rho_f$	$1.0 \times 10^3$	$\text{kg m}^{-3}$
fluid's dynamic viscosity	$\mu$	$1.0 \times 10^{-3}$	Pas
inlet flow rate	$q$	See table 5	$\mu\text{l min}^{-1}$
effective interface thickness	$b^*$	$0.6141w = 307.05$	$\mu\text{m}$
channel's height-to-length aspect ratio	$\epsilon = h_0/\ell$	0.003	–
channel's height-to-width aspect ratio	$\delta = h_0/w$	0.06	–
reduced Reynolds number	$\hat{Re} = \epsilon \rho q / (w \mu)$	See table 5	–
FSI parameter	$\beta = \mathcal{I}_1 \mathcal{P}_c \xi / (E h_0)$	See table 5	–
solid's inertia coefficient	$\theta_I = \epsilon \hat{Re} \beta b^* \rho_s / (\ell \rho_f)$	See table 5	–
deformation-induced tension coefficient	$\theta_t(T) = \tilde{\theta}_t \int_0^1 \frac{1}{2} \left( \frac{\partial \bar{H}}{\partial Z} \right)^2 dZ$	Variable ( $\tilde{\theta}_t$ in table 5)	–

Table 4: The dimensional and dimensionless parameters of the 1D FSI model.

$Q(Z, T) = \int_0^{\bar{H}(Z, T)} V_Z^{2D}(Y, Z, T) dY$ , into the formulation. Invoking a von Kármán–Pohlhausen approximation (Pohlhausen, 1921) (see also, *e.g.*, (White, 2006, §4-6.5) or (Panton, 2013, p. 541)), we assume a parabolic velocity profile across any deformed cross-section of the channel:

$$V_Z^{2D}(Y, Z, T) = \frac{6QY[\bar{H}(Z, T) - Y]}{\bar{H}^3(Z, T)}. \quad (5.1)$$

The kinematic boundary conditions at the top wall requires that

$$V_Y^{2D}|_{Y=\bar{H}} = \frac{\partial \bar{H}}{\partial T}. \quad (5.2)$$

Making equations (3.1a) and (3.1d) dimensionless, neglecting  $x$ -dependent terms and small terms, and integrating over  $Y$ , we obtain

$$\frac{\partial Q}{\partial Z} + \frac{\partial \bar{H}}{\partial T} = 0, \quad (5.3a)$$

$$\hat{Re} \frac{\partial Q}{\partial T} + \hat{Re} \frac{6}{5} \frac{\partial}{\partial Z} \left( \frac{Q^2}{\bar{H}} \right) = -\bar{H} \frac{\partial P}{\partial Z} - \frac{12Q}{\bar{H}^2}, \quad (5.3b)$$

where the no slip boundary conditions have been applied at  $Y = 0$  and  $Y = \bar{H}$ . Note equations (5.3) were also previously derived by Stewart et al. (2009) and Inamdar et al. (2020).

Equations (5.3a), (5.3b), (4.12) and (4.10) define a 1D FSI model. In this work, we consider the case in which the flow rate at the inlet is fixed, while the pressure at the outlet is set to gauge, *i.e.*,

$$Q(0, T) = 1, \quad P(1, T) = 0. \quad (5.4)$$

Also, there are no displacements at the inlet and the outlet of the channel:

$$\bar{U}_Y(0, T) = \bar{U}_Y(1, T) = 0 \quad \Rightarrow \quad \bar{H}_Y(0, T) = \bar{H}_Y(1, T) = 1. \quad (5.5)$$

Initially, we assume the wall is undeformed and the flow is uniform through the channel, *i.e.*,

$$Q(Z, 0) = 1, \quad \bar{U}_Y(Z, 0) = 0 \quad \Rightarrow \quad \bar{H}_Y(Z, 0) = 1. \quad (5.6)$$

## 5.1 Exemplar cases and preview of results

The remainder of this paper is concerned with the steady-state features, the dynamic response, and also the linear stability of the non-flat steady state of the proposed 1D FSI model. To explore these issues, we have chosen exemplar cases with typical dimensional and dimensionless values given in table 4 and table 5. The values for the geometrical and material properties are taken and/or modified from (Gervais et al., 2006). The long and shallow microchannels are assumed fabricated via soft lithography, with a thick top wall. The leading-order steady response of such microchannels has been solved by Wang and Christov (2019), according to which,  $\mathcal{I}_1 = 0.542754$  and  $\xi = w$  for calculating  $\beta$  in table 5.

Case	$E$ (MPa)	$q$ ( $\mu\text{l min}^{-1}$ )	$\hat{Re}$ (-)	$\beta$ (-)	$\theta_I$ (-)	$\tilde{\theta}_t$ (-)
C1	1	1500	0.15	0.1256	$1.7360 \times 10^{-6}$	$5.6245 \times 10^{-9}$
C2	1	6000	0.60	0.5026	$2.7775 \times 10^{-5}$	$5.6245 \times 10^{-9}$
C3	1	9000	0.90	0.7538	$6.2495 \times 10^{-5}$	$5.6245 \times 10^{-9}$
C4	2	1500	0.15	0.0628	$8.6798 \times 10^{-7}$	$5.6245 \times 10^{-9}$
C5	2	6000	0.60	0.2513	$1.3888 \times 10^{-5}$	$5.6245 \times 10^{-9}$
C6	2	9000	0.90	0.3769	$3.1247 \times 10^{-5}$	$5.6245 \times 10^{-9}$

Table 5: The dimensional and dimensionless parameters for the exemplar cases considered.

Similar to the experiments of Verma and Kumaran (2013), cases C1 to C3 and C4 to C6 summarized in table 5 are each based on a single microchannel, operated under different flow conditions. As catalogued in table 6, the steady and dynamic responses of the new 1D FSI model match several experimental observations qualitatively, which indicates that the proposed model can provide unique insights into this unstable FSI problem. However, we cannot perform direct quantitative comparisons between our 1D model and the experiments of Verma and Kumaran (2013), for the following reasons. First, the experiments’ soft wall was compressed upon a rigid outer surface, unlike our model wherein a soft wall that bulges outwards in an unconstrained manner (being stress-free on its outer surface). Further, in the experiments, the wall thickness was comparable to the channel’s width, with two side walls made rigid. Consequently, the deformation field within the compliant wall in the microchannels fabricated by Verma and Kumaran (2013) is described by a different leading-order theory of the flow-induced deformation than the theories considered herein (recall section 4). At this time, it is not clear whether an exact solution (along the lines of Wang and Christov (2019)) could be obtained for the deformation in the configuration fabricated by Verma and Kumaran (2013). The main difference would be in the definition of  $\beta$ . Nevertheless, since the experiments did consider long and shallow microchannels with a slender deformable wall, the assumptions made in sections 3 and 4 apply. Therefore, the FSI *physics* in these experiments are expected to be captured by the theoretical framework proposed herein. Indeed, as discussed by Verma and Kumaran (2013), the FSI-induced instabilities are generic, thus are not expected to be an “accidental” phenomenon occurring only in some specific experimental devices. It follows that our qualitative comparisons below are meaningful and useful for validating the proposed 1D FSI model.

## 6 Base state: features of the inflated microchannel at steady state

At steady state, all the time derivatives vanish. From equation (5.3a), we have  $Q \equiv 1$ , upon imposing the fixed-flux upstream boundary condition from equation (5.4). The remaining equations (4.12), (4.10) and (5.3b), together with the unsatisfied boundary conditions from equations (5.4) and (5.5), constitute a nonlinear two-point boundary value problem (Keller, 1976). This nonlinear system is solved using the `newton_krylov` routine from the SciPy stack (Virtanen et al., 2020), following the procedure described in the supplementary materials.

Also, note that equations (4.12), (4.10) and (5.3b) can be combined to form a single equation, in terms



	Experimental observation	Proposed 1D FSI model behavior
Steady	<ul style="list-style-type: none"> <li>• Wall deformation is nonuniform along the streamwise direction.</li> <li>• There is a sharp diverging section after the channel entrance, followed by a longer converging section tapering towards the outlet.</li> </ul>	<ul style="list-style-type: none"> <li>• The steady-state pressure and deformation profiles vary along streamwise direction.</li> <li>• For weak axial tension, the channel expands sharply near the inlet, reaching a maximum deformation. Then, the deformation tapers out towards the outlet. This effect is due to the governing equation of the fluid–solid interface exhibiting a boundary-layer-like behavior for <math>\theta_t \ll 1</math>.</li> </ul>
Dynamic	<ul style="list-style-type: none"> <li>• Dye injected in the flow oscillates/breaks up at <math>Re \simeq 100</math> and <math>\hat{Re} \simeq 1</math>. The dye is observed to break up first in the converging section near the channel outlet.</li> <li>• In the mixing experiments, vigorous mixing is observed downstream in the converging section at <math>Re \simeq 100</math> and <math>\hat{Re} \simeq 1</math>.</li> <li>• Under the same flow rate, the mixing in the more compliant channel is observed to be more complete.</li> <li>• The wall oscillates as the dye breakup (instability) is observed.</li> </ul>	<ul style="list-style-type: none"> <li>• The base (steady) solution becomes linearly unstable to infinitesimal perturbations at <math>Re \simeq 100</math> and <math>\hat{Re} \simeq 1</math>.</li> <li>• The global unstable modes are found to be highly oscillatory, with frequencies close to the natural frequency of the wall. The corresponding eigenfunctions are highly oscillatory in space, with the shape changing more dramatically near the outlet than that near the inlet.</li> <li>• Under the same flow rate, the more compliant channel has larger growth rate for the most unstable mode.</li> <li>• Self-sustained wall oscillations can be triggered in the linearly unstable cases. The wall oscillations have a peak frequency close to the natural frequency of the wall, and are found to be more violent near the channel outlet.</li> </ul>

Table 6: Qualitative comparison between the experimental observations of [Verma and Kumaran \(2013\)](#) and the predictions of the proposed global 1D FSI model.

of the steady-state deformed height  $\bar{H}_0$ , written as

$$\frac{6}{5}\hat{Re}\frac{1}{\bar{H}_0^3}\frac{d\bar{H}_0}{dZ} = \frac{1}{\beta}\left(\frac{d\bar{H}_0}{dZ} - \theta_t\frac{d^3\bar{H}_0}{dZ^3}\right) + \frac{12}{\bar{H}_0^3}. \quad (6.1)$$

The boundary conditions for this third-order nonlinear ordinary differential equation (ODE) are

$$\bar{H}_0(Z=0) = \bar{H}_0(Z=1) = 1, \quad \left.\frac{d^2\bar{H}_0}{dZ^2}\right|_{Z=1} = 0, \quad (6.2)$$

which correspond to zero displacement imposed at  $Z = 0, 1$ , along with the gauge-pressure boundary condition at the outlet.

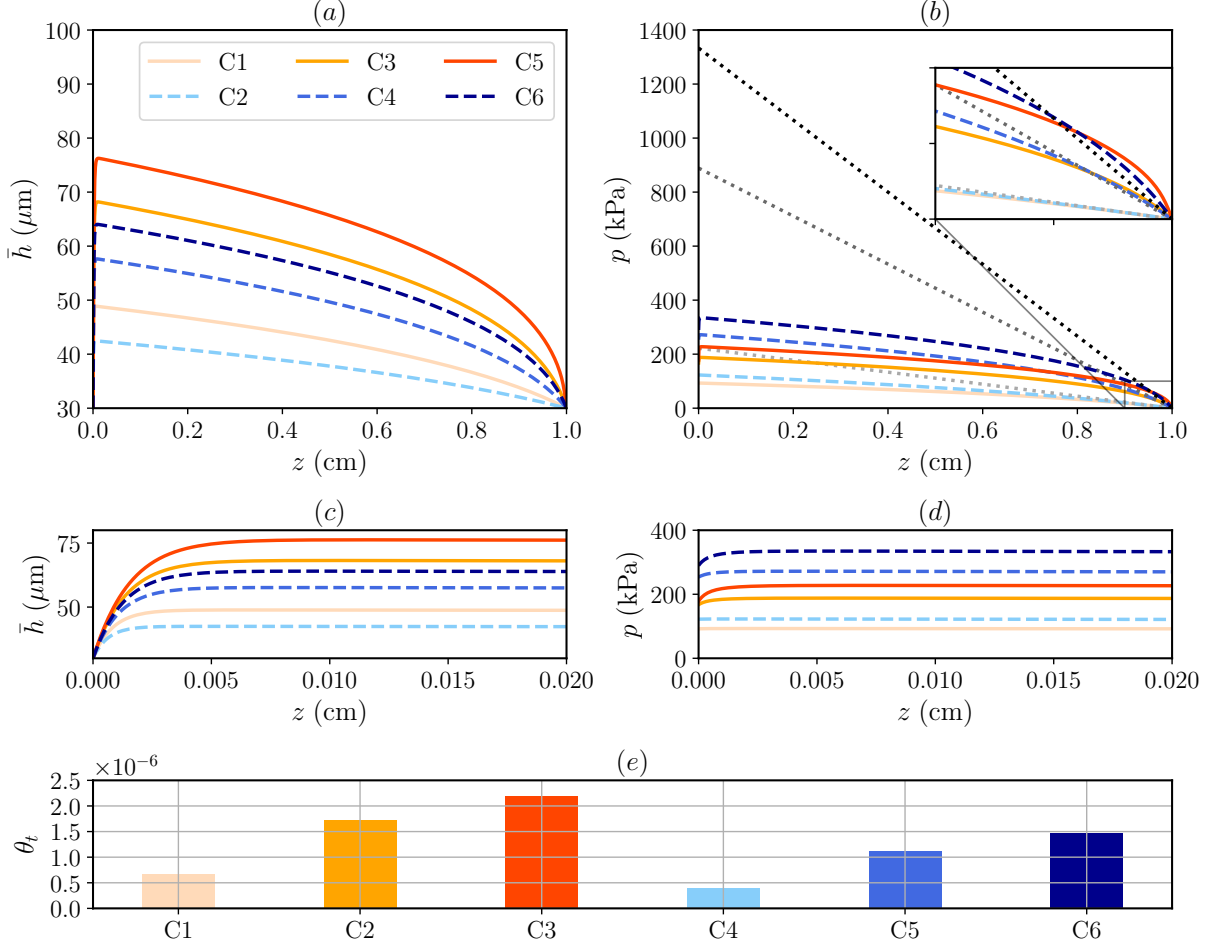


Figure 3: The steady-state response for the exemplar cases from table 5, for flow rates or  $q = 1500, 6000, 9000 \mu\text{l min}^{-1}$  (higher  $q$  corresponds to darker curves). (a) The variation of the deformed channel height along  $z$ . (b) The pressure distribution along  $z$ , with the inset window showing a zoom-in view near the  $z = \ell$ . The dotted lines show the Hagen–Poiseuille law for a rigid channel (linearly variation of  $p$  along  $z$ ). Panels (c) and (d) show zoomed-in views for  $\bar{h}$  and  $p$  near the inlet,  $z = 0$ , respectively. (e) The computed  $\theta_t$  of the exemplar cases from table 5.

The steady responses of the exemplar cases from table 5 are shown in figure 3. The nonuniform deformation of the channel height is shown in figure 3(a), along with a zoom-in view near the inlet given in figure 3(c). The channel inflates more for larger flow rates and/or for softer walls (*i.e.*, with smaller  $E$ ). For each case, there is a sharp diverging section near the channel inlet, and a much longer converging section connecting to the channel outlet, which agrees with the experimental observations of Verma and Kumaran (2013). As for the pressure distribution, figure 3(b) shows that the compliance of the wall leads to a non-uniform pressure gradient so that the pressure varies nonlinearly with  $z$ . Furthermore, compared to the case of flow in the rigid channel, the total pressure drop is reduced significantly due to the expanded cross-sectional area resulting from the deformation of the wall. This phenomenon has been addressed and analyzed, considering different geometrical configurations and elastic response, but typically limited to the case of  $\hat{Re} \rightarrow 0$  (see, *e.g.*, Christov, 2022). However, our proposed 1D FSI model pushes the limit to  $\hat{Re} = \mathcal{O}(1)$ . Figure 3(d) also zooms into the neighborhood of the channel inlet. As the flow rate increases, a small region of positive pressure gradient appears. The reason for this effect is that, the sharp expansion of the channel’s cross-section near the inlet makes the local velocity drop quickly (recall that  $Q \equiv 1$  at steady state), and the positive pressure

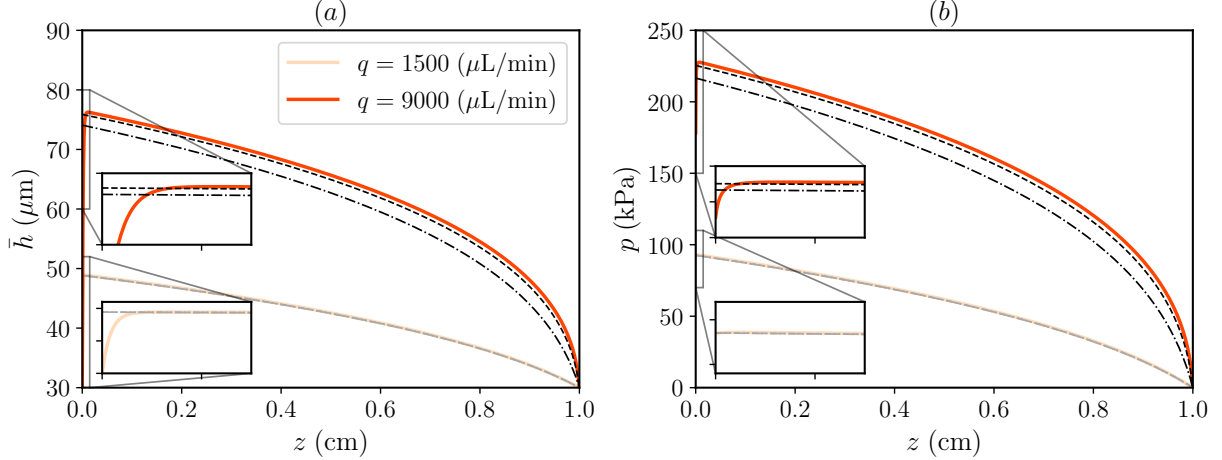


Figure 4: Comparison between the numerical solutions of the proposed 1D FSI model and previously reported analytical results for the exemplar cases of C1 and C3. (a) the deformed channel height along  $z$ . (b) the pressure distribution along  $z$ . The solid curves represent the numerical simulation of the 1D FSI model at steady state. The dash-dotted curves represent the results calculated by equation (6.3) with  $\hat{Re} = 0$  and  $\theta_t = 0$ . The dashed curves are calculated from equation (6.4), in which  $\theta_t = 0$  but  $\hat{Re} = \mathcal{O}(1)$ .

gradient aids in the deceleration of the flow (Inamdar et al., 2020; Wang and Christov, 2021). Finally, the deformation-induced weak tension coefficients of the exemplar cases are shown in figure 3(e). We observe that  $\theta_t$  increases as the flow rate increases because higher flow rates induce larger deformations. Moreover, for the same flow conditions, it is observed that  $\theta_t$  is larger when the wall is more compliant.

Next, to address the effect of  $\hat{Re}$  and  $\theta_t$ , we compare the numerical results of the current 1D FSI model with previous reported analytical results. At this stage,  $\theta_t$  is fixed to be the corresponding values from figure 3(e). First, taking  $\hat{Re} \rightarrow 0$  and neglecting  $\theta_t$ , the pressure distribution and the deformation at steady state (Wang and Christov, 2021) are

$$P_0(Z) = \frac{1}{\beta} \left\{ [48\beta(1-Z) + 1]^{1/4} - 1 \right\}, \quad \bar{H}_0(Z) = 1 + \beta P_0(Z). \quad (6.3)$$

Equation (6.3) is the essentially the same as the model proposed by Gervais et al. (2006). However, in the current theoretical framework,  $\beta$  is obtained by solving an appropriate linear elasticity problem, instead of being calibrated by an experiment. Second, if only  $\theta_t$  is neglected but  $\hat{Re} = \mathcal{O}(1)$ , the steady-state pressure distribution (Wang and Christov, 2021) is

$$P_0(Z) \left[ 1 + \frac{3}{2}\beta P_0(Z) + \beta^2 P_0^2(Z) + \frac{1}{4}\beta^3 P_0^3(Z) - \frac{6}{5}\hat{Re}\beta \right] = 12(1-Z), \quad \bar{H}_0(Z) = 1 + \beta P_0(Z). \quad (6.4)$$

Observe that equation (6.4) reduces to equation (6.3) for  $\hat{Re} \rightarrow 0$ . Finally, we mention that if both  $\theta_t, \hat{Re} \neq 0$ , equation (6.1) is essentially a singular perturbation problem, which can be solved using the method of matched asymptotic expansions. Specifically, Wang and Christov (2021) showed that there exists a boundary layer near  $Z = 0$  of thickness  $\mathcal{O}(\theta_t^{1/2})$ , and obtained a matched asymptotic solution, which is too lengthy to summarize here.

In figure 4, we show a comparison between the steady-state solution obtained by numerical simulation of the 1D FSI model and the analytical results mentioned above. For a low flow rate, with  $\hat{Re} = 0.15$ , the fluid inertia is not important, thus the numerical results agree well with the analytical results, except near the inlet. In contrast, for a high flow rate, with  $\hat{Re} = 0.9$ , the results neglecting the effect of  $\hat{Re}$  (based on equation (6.3)) tend to underestimate the channel deformation and the pressure distribution. Since equations (6.3) and (6.4) do not take into account the weak tension effect, the no-displacement restriction at the inlet is not satisfied. With  $\theta_t$  included, whether the flow rate is low or high, a short diverging section of the channel height emerges near the inlet, indicating the feature of a boundary layer problem described above.

## 7 Linear stability of the inflated base state

In this section, we address the linear stability of the base (steady-state) solutions obtained in section 6. We have shown, in figure 3, that both the deformation and the pressure gradient are nonuniform along  $z$  in the inflated (non-flat) base state. This observation makes the linear stability problem nontrivial, as the linearized operators have variable coefficients and are not self-adjoint. The key question that this section will address is: is the non-flat base state linearly stable to infinitesimal perturbations?

To answer this question, we perturb the base state with an infinitesimal disturbance as:

$$Q(Z, T) = Q_0 + \alpha \hat{Q}(Z, T), \quad \bar{H}(Z, T) = \bar{H}_0(Z) + \alpha \hat{H}(Z, T), \quad (7.1)$$

with  $\alpha \ll 1$ . Note  $Q_0 = 1$  for fixed flux upstream. Substituting the above into the governing equations (5.3) and (4.12), and keeping terms up to  $\mathcal{O}(\alpha)$ , we get the following linear evolution equations:

$$\frac{\partial \hat{H}}{\partial T} + \frac{\partial \hat{Q}}{\partial Z} = 0, \quad (7.2a)$$

$$\begin{aligned} \frac{\hat{R}e\beta}{\bar{H}_0} \frac{\partial \hat{Q}}{\partial T} + \frac{6}{5} \hat{R}e\beta \left[ \left( \frac{3Q_0^2}{\bar{H}_0^4} \frac{d\bar{H}_0}{dZ} - \frac{Q_0^2}{\bar{H}_0^3} \frac{\partial}{\partial Z} \right) \hat{H} + \left( -\frac{2Q_0}{\bar{H}_0^3} \frac{d\bar{H}_0}{dZ} + \frac{2Q_0}{\bar{H}_0^2} \frac{\partial}{\partial Z} \right) \hat{Q} \right] \\ + \theta_I \frac{\partial^3 \hat{H}}{\partial Z \partial T^2} + \frac{\partial \hat{H}}{\partial Z} - \theta_t \frac{\partial^3 \hat{H}}{\partial Z^3} + 12\beta \left( \frac{\hat{Q}}{\bar{H}_0^3} - \frac{3Q_0}{\bar{H}_0^4} \hat{H} \right) = 0. \end{aligned} \quad (7.2b)$$

We further note that  $\theta_t$  in the above equation is fixed to be the steady-state value rather than computed from equation (4.16), *i.e.*, we have neglected any modifications of  $\theta_t$  introduced by the initial perturbations. It can be shown (see section 8.1) that this effect is negligible.

In this work, we only consider the asymptotic behavior of infinitesimal initial perturbations, *i.e.*, the modal analysis. To this end, we write

$$\hat{Q}(Z, T) = \tilde{Q}(Z) e^{-i\omega_G T}, \quad \hat{H}(Z, T) = \tilde{H}(Z) e^{-i\omega_G T}. \quad (7.3)$$

Since the base state is non-flat, the eigenfunctions  $\tilde{Q}$  and  $\tilde{H}$  are not homogeneous in  $Z$ . Then,  $\omega_G \in \mathbb{C}$  denotes the “global” growth/decay rate of the eigenmode (Huerre and Monkewitz, 1990).

For computational convenience, equation (7.2) is re-written in matrix form as

$$\underbrace{\begin{pmatrix} 0 & \frac{d}{dZ} \\ \mathcal{L}_H & \mathcal{L}_Q \end{pmatrix}}_{\mathbf{A}} \underbrace{\begin{pmatrix} \tilde{H} \\ \tilde{Q} \end{pmatrix}}_{\boldsymbol{\psi}} = i\omega_G \underbrace{\begin{pmatrix} 1 & 0 \\ 0 & \frac{\hat{R}e\beta}{\bar{H}_0} - \theta_I \frac{d^2}{dZ^2} \end{pmatrix}}_{\mathbf{B}} \underbrace{\begin{pmatrix} \tilde{H} \\ \tilde{Q} \end{pmatrix}}_{\boldsymbol{\psi}}, \quad (7.4)$$

with the operators  $\mathcal{L}_H$  and  $\mathcal{L}_Q$  defined as

$$\mathcal{L}_H = \frac{6}{5} \hat{R}e\beta \left( \frac{3Q_0^2}{\bar{H}_0^4} \frac{d\bar{H}_0}{dZ} - \frac{Q_0^2}{\bar{H}_0^3} \frac{d}{dZ} \right) + \frac{d}{dZ} - \theta_t \frac{d^3}{dZ^3} - \frac{36\beta Q_0}{\bar{H}_0^4}, \quad (7.5a)$$

$$\mathcal{L}_Q = \frac{6}{5} \hat{R}e\beta \left( -\frac{2Q_0}{\bar{H}_0^3} \frac{d\bar{H}_0}{dZ} + \frac{2Q_0}{\bar{H}_0^2} \frac{d}{dZ} \right) + \frac{12\beta}{\bar{H}_0^3}. \quad (7.5b)$$

Note that  $\mathcal{L}_H$  and  $\mathcal{L}_Q$  are linear operators with *non-constant* coefficients, as a consequence of the non-flat base state. Also note in  $\mathbf{B}$ ,  $\theta_I d^2 \tilde{Q}/dZ^2$  originates from  $\theta_I \partial^3 \hat{H}/(\partial Z \partial T^2) = \theta_I \partial^3 \hat{Q}/(\partial Z^2 \partial T)$ , using equation (7.2a).

Since the base state has satisfied all the boundary conditions from equations (5.4) and (5.5). The boundary conditions for the infinitesimal perturbations are homogeneous:

$$\tilde{Q}|_{Z=0} = \frac{d\tilde{Q}}{dZ} \Big|_{Z=0} = \frac{d\tilde{Q}}{dZ} \Big|_{Z=1} = 0, \quad (7.6a)$$

$$\tilde{H}|_{Z=0} = \tilde{H}|_{Z=1} = \left. \frac{d^2 \tilde{H}}{dZ^2} \right|_{Z=1} = 0. \quad (7.6b)$$

The first boundary condition is deduced from the fixed flux upstream boundary condition, while the boundary conditions in terms of  $\tilde{H}$  correspond to the no-displacement restrictions at both ends and the outlet pressure set to gauge. The remaining two boundary conditions on  $\tilde{Q}$  are derived from the equation (5.3a) by imposing zero displacement at the channel inlet and outlet.

Equation (7.4) subject to equation (7.6) gives rise to a generalized eigenvalue problem, which can be solved numerically using the Chebyshev pseudospectral method (see the [supplementary materials](#) for details). For all the eigenmodes resolved, if the corresponding  $\text{Im}(\omega_G) > 0$ , we say the non-flat base state of the 1D FSI system is linearly unstable to infinitesimal disturbances.

## 7.1 Eigenspectra of the exemplar cases

Here, it is illustrative to plot *dimensional* quantities to show how a corresponding physical system would behave. To this end, we write the dimensional frequency as

$$f_g = \frac{\omega_G}{2\pi\mathcal{T}_f} = \frac{\omega_G q}{2\pi\ell w h_0}. \quad (7.7)$$

Note that  $f_g \in \mathbb{C}$ , such that  $\text{Re}(f_g)$  is the oscillatory frequency of the corresponding eigenmode, *i.e.*,  $[\tilde{H}, \tilde{Q}]^T$  in our formulation, while  $\text{Im}(f_g)$  is the eigenmode's grow/decay time constant.

On the other hand, since equation (4.12) essentially represents a mechanical oscillator, the dimensionless and dimensional natural frequency of the oscillator, denoted as  $F_N$  and  $f_n$  respectively, can be approximated as

$$F_N = \frac{1}{2\pi\sqrt{\theta_I}}, \quad f_n = \frac{F_N}{\mathcal{T}_f} = \frac{F_N q}{\ell w h_0}. \quad (7.8)$$

Unlike  $f_g$ , both  $F_N, f_n \in \mathbb{R}$ . Also note that, equation (7.8) does not take the tension effect into account, but since tension is weak, we believe equation (7.8) provides a good approximation to the natural frequency of the system.

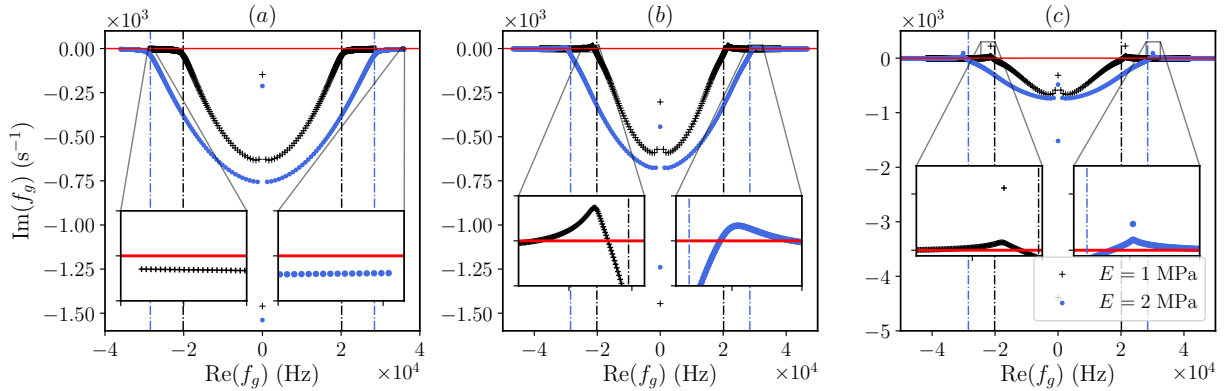


Figure 5: Eigenspectra of the exemplar cases from table 5: (a)  $q = 1500 \text{ } \mu\text{l min}^{-1}$ ; (b)  $q = 6000 \text{ } \mu\text{l min}^{-1}$ ; (c)  $q = 9000 \text{ } \mu\text{l min}^{-1}$ . The symbols represent the discrete eigenvalues for  $E = 1 \text{ MPa}$  and  $E = 2 \text{ MPa}$  respectively. The red horizontal line mark the position of real axis, *i.e.*,  $\text{Im}(f_g) = 0$ . The dash-dotted lines mark the natural frequencies calculated by equation (7.8). The insets in each panel have the same vertical axes.

In figure 5, we show the calculated eigenspectra for the six exemplar cases from table 5. First, observe that the eigenspectra are symmetric about the imaginary axis in the complex plane. This symmetry is a consequence of the formulation of the generalized eigenvalue problem (see equation (7.4)), as the matrix  $\mathbf{A}$

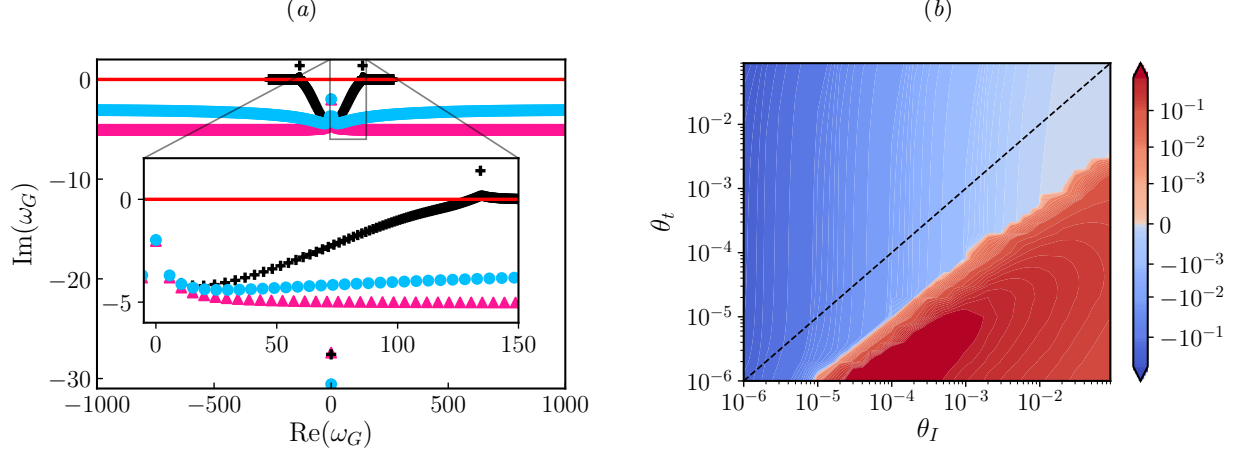


Figure 6: (a) Comparison of the eigenspectra of the case with  $\theta_I \ll 1$  and  $\theta_t \ll 1$  (+), the case with  $\theta_t \ll 1$  but  $\theta_I = 0$  ( $\bullet$ ), and the case with  $\theta_I = 0$  and  $\theta_t = 0$  ( $\blacktriangle$ ). The dimensionless parameters are taken as per case C3 in table 5. (b) Contour plot of  $\text{Im}(\omega_G)$  of the least stable mode as a function of  $\theta_I$  and  $\theta_t$ , with  $\hat{Re}$  and  $\beta$  taken from case C3 in table 5. The dashed line marks  $\theta_I = \theta_t$ .

on the left-hand side is purely real, while the matrix  $i\mathbf{B}$  on the right-hand side is purely imaginary. This symmetry is also a feature of the eigenvalue analyses in (Inamdar et al., 2020; Wang and Christov, 2020).

Second, the 1D FSI system transitions from stability (panel (a)) to instability (panels (b) and (c)) as the flow rate is increased. The fluid inertia becomes more prominent as the flow rate is increased, indicated by the magnitude of  $\hat{Re}$ , which is associated with the nonlinear terms on the left-hand side of equation (5.3b). For the six exemplar cases from table 5, we observe that the linear instability typically occurs for  $\hat{Re} \simeq 1$ , or equivalently  $Re \simeq 100$ , which is close to the values reported for the microchannel experiments showing instability (Verma and Kumaran, 2013).

Third, it is observed that the unstable regions in figure 5(b) and (c) are close to the natural frequency, indicating that the instabilities are related to the resonance of the wall. Due to the weak solid inertia, the natural frequency calculated from equation (7.8), as well as  $\text{Re}(f_g)$  in the unstable region, is as high as  $\simeq 10^4$  Hz. This fact also matches the local linear stability analysis of Verma and Kumaran (2013), who reported that the least stable mode oscillates at a frequency on the order of  $10^4$  Hz. Moreover, one of the common features of the eigenspectra in figure 5 is that,  $\text{Im}(f_g)$  is larger at higher frequencies (*i.e.*, at larger  $|\text{Re}(f_g)|$ ). This observation indicates that, apart from those modes that grow for the given flow conditions, the stable modes that oscillate with higher frequency will decay slower, which highlights the *computational* stiffness of the 1D FSI system.

Lastly, the compliance of the wall does influence the shape of the eigenspectra. Since the stiffer wall has a larger natural frequency, its unstable region is located at higher frequencies than its softer counterpart. Note that in figure 5, the two zoom-in insets in each panel have the same range for the vertical axis. Then it can be shown that the more compliant wall has the larger growth rate (or the smaller decay rate in the linearly stable case) for the least stable mode, which could be related to the experimental observations that the softer microchannel is more prone to instabilities (Verma and Kumaran, 2013).

Since both  $\theta_I$  and  $\theta_t$  are small quantities in the solid mechanics equation (4.12), it would be interesting to show a comparison of the linear stability between cases either  $\theta_I = 0$  or  $\theta_t = 0$ . We consider three different such cases: (i)  $\theta_I \ll 1$  and  $\theta_t \ll 1$ ; (ii)  $\theta_I = 0$  and  $\theta_t \ll 1$ ; (iii)  $\theta_I = 0$  and  $\theta_t = 0$ . The base states of both case (i) and (ii) are the same, governed by equation (6.1). However, in case (iii), the system cannot satisfy  $\bar{H}(0) = 0$ , thus the corresponding base state should be taken from equation (6.4). As shown in figure 6(a), we observe that even though the solid inertia and tension are weak in the system, the inclusion of these weak effects changes the eigenspectrum fundamentally. The non-flat base state from equation (6.4) is shown to be linearly stable. With only  $\theta_t \neq 0$ , case (ii) can predict linear stability only while the case (i) with both  $\theta_I, \theta_t \neq 0$  is linearly unstable. Furthermore, as shown in both case (ii) and (iii), for  $\theta_I = 0$ , the eigenmodes oscillate with higher frequencies. The reason is that, in this case, the natural frequency  $F_N \rightarrow \infty$  as  $\theta_I \rightarrow 0$ .



Case	Pure decay mode	Least stable mode
C1	$-5.5501i$	—
C2	$-2.8538i$	$202.3535 + 0.1393i$
C3	$-1.9762i$	$134.2670 + 1.3892i$
C4	$-8.0068i$	—
C5	$-4.1750i$	$284.8114 + 0.0637i$
C6	$-3.0423i$	$189.2292 + 0.5867i$

Table 7: The dimensionless eigenvalues,  $\omega_G$ , for the pure decay modes and for the least unstable modes of the exemplar cases from table 5.

To further investigate the effect of  $\theta_I$  and  $\theta_t$ , we calculated the growth/decay rate of the least stable mode by taking different combination of  $\theta_I$  and  $\theta_t$ , fixing  $\tilde{Re}$  and  $\beta$  as the values corresponding to case C3. As shown in panel (b) of figure 6, for both  $\theta_I$  and  $\theta_t$  across five orders, linear instabilities are only observed when  $\theta_I$  is at least one order larger than  $\theta_t$ . Since the dimensionless phase speed of the transverse waves along the fluid–solid interface is  $\sqrt{\theta_t/\theta_I}$ , then the linear instability occurs when the transverse waves propagate (much) slower than the flow.

## 7.2 Eigenfunctions of the exemplar cases

Each eigenvalue is associated with an eigenfunction pair, *i.e.*,  $[\tilde{H}, \tilde{Q}]^T$  via equation (7.4). For the eigenvalues with larger  $|\text{Re}(\omega_G)|$ , the corresponding eigenfunctions are more oscillatory in space. For example, for the purely decay mode with  $\text{Re}(\omega_G) = 0$ , the corresponding eigenfunctions are found to be purely real and non-oscillatory, as shown in figure 7. However, for the least stable modes of the linearly unstable cases from table 5, as shown in figure 8, with  $|\text{Re}(\omega_G)| \gg 1$ , the corresponding eigenfunctions are highly oscillatory in space. The corresponding eigenvalues for the eigenfunctions in figure 7 and figure 8 are tabulated in table 7.

We do not tabulate the least stable modes of the linearly stable cases in table 7 because it is hard to pick out the least stable mode due to the limitation of the numerical method. In that case, we observe that the least stable mode is always the farthest eigenvalue away from the imaginary axis, if computed with the Chebyshev pseudospectral method using different number of Gauss–Lobatto points  $N$ . In principle, there are infinite number of eigenvalues in the 1D FSI system, resolving all of which would require an infinite number of Gauss–Lobatto points. Unfortunately,  $N$  cannot be arbitrarily large because matrices in equation (7.4) will become ill-conditioned.

Let’s take a closer look at the eigenfunctions of the least stable modes in figure 8. For all the cases, both  $\tilde{H}$  and  $\tilde{Q}$  exhibit much larger oscillations near the channel outlet ( $Z = 1$ ), which echos the experimental observation that the instabilities were always first observed near the outlet in the converging section of the microchannel (Verma and Kumaran, 2013). Furthermore, with larger growth rate, the difference in oscillations between the outlet and the inlet is more prominent (comparing C2 and C3, or C5 and C6).

The wavy forms of the eigenfunctions in figure 8 further inspire us to conduct a Fourier transform in space for each case. We have used the SciPy’s `fft` routine with a Blackman window. The results are summarized in figure 9 and the abscissa represents the reciprocal of the dimensionless wave length, denoted by  $\Lambda = \lambda/\ell$ . Here,  $\lambda$  is the dimensional wave length. Interestingly, there are always two peaks for all the cases. The major peak is located at  $1/\Lambda \simeq 100$ , meaning the dominant wavelength is on the order of the channel height (recall  $\ell/h_0 \approx 333$ ). This observation could be related to the results of the local linear stability analysis of Verma and Kumaran (2013), who found that the most unstable modes have a wavelength comparable to the channel height.

## 8 Dynamic response of the microchannel

In this section, we solve the 1D FSI model, by discretizing the governing equations in space and time, to investigate the dynamic responses. The spatial discretization is based on the Chebyshev pseudospectral method (Boyd, 2000; Shen et al., 2011), while the “Newmark- $\beta$ ” method (Subbaraj and Dokainish, 1989)

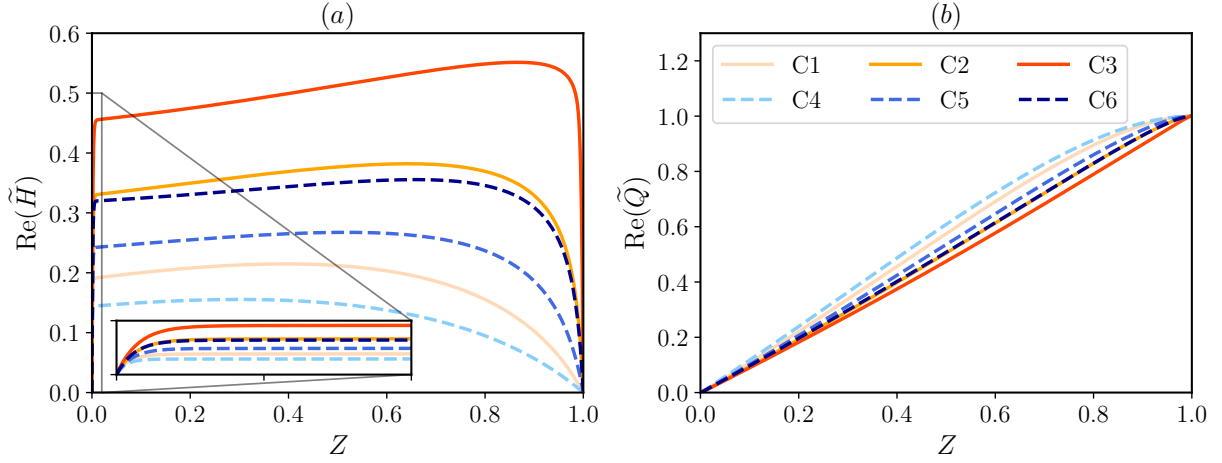


Figure 7: The eigenfunctions of the pure decay eigenmodes of the six exemplar cases from table 5. The eigenfunctions have been scaled by keeping  $\max |\tilde{Q}| = 1$ .

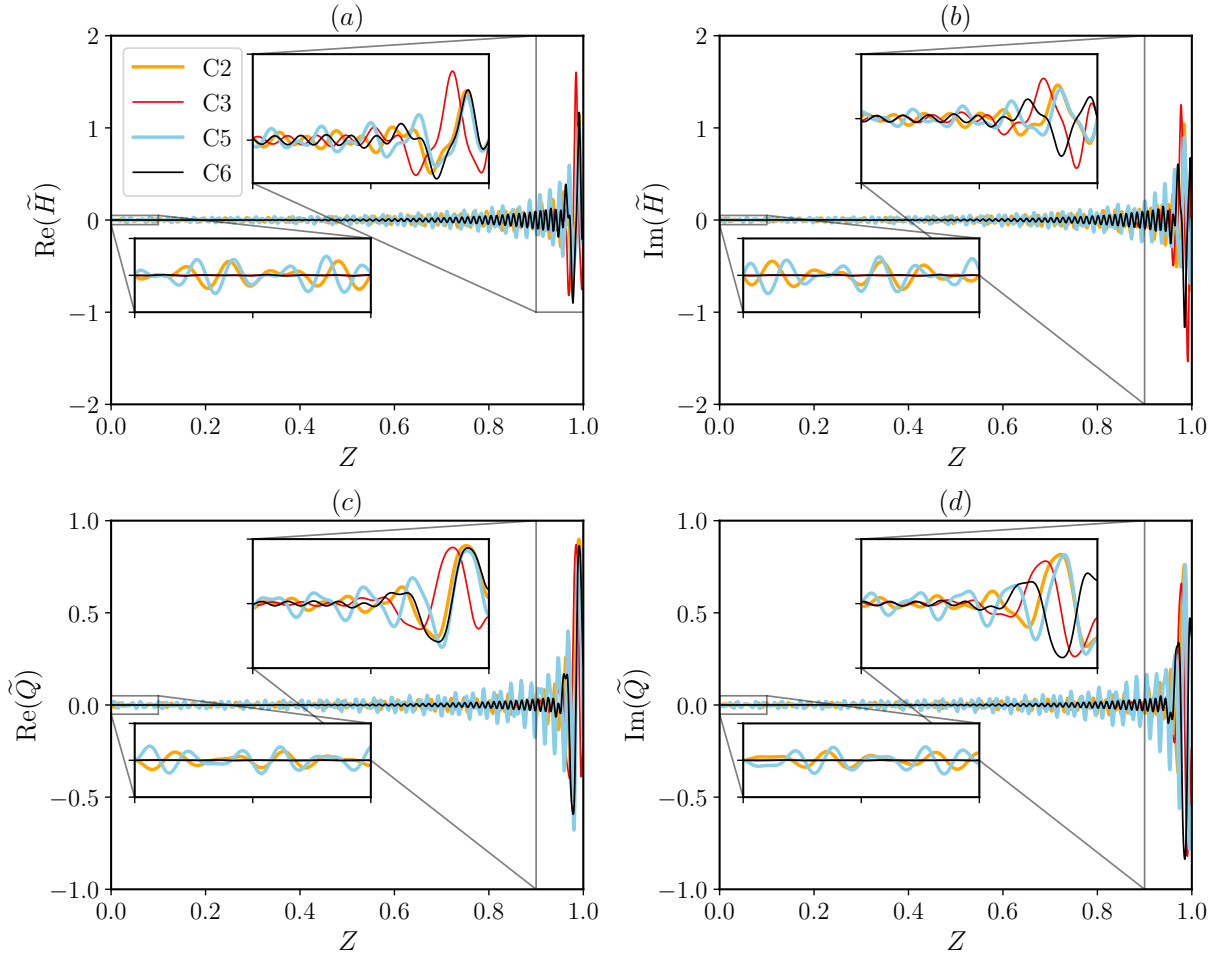


Figure 8: The eigenfunctions of the least stable modes for the linearly unstable cases, *i.e.*, C2, C3, C5 and C6 in table 5. The eigenfunctions have been scaled by keeping  $\max |\tilde{Q}| = 1$ .

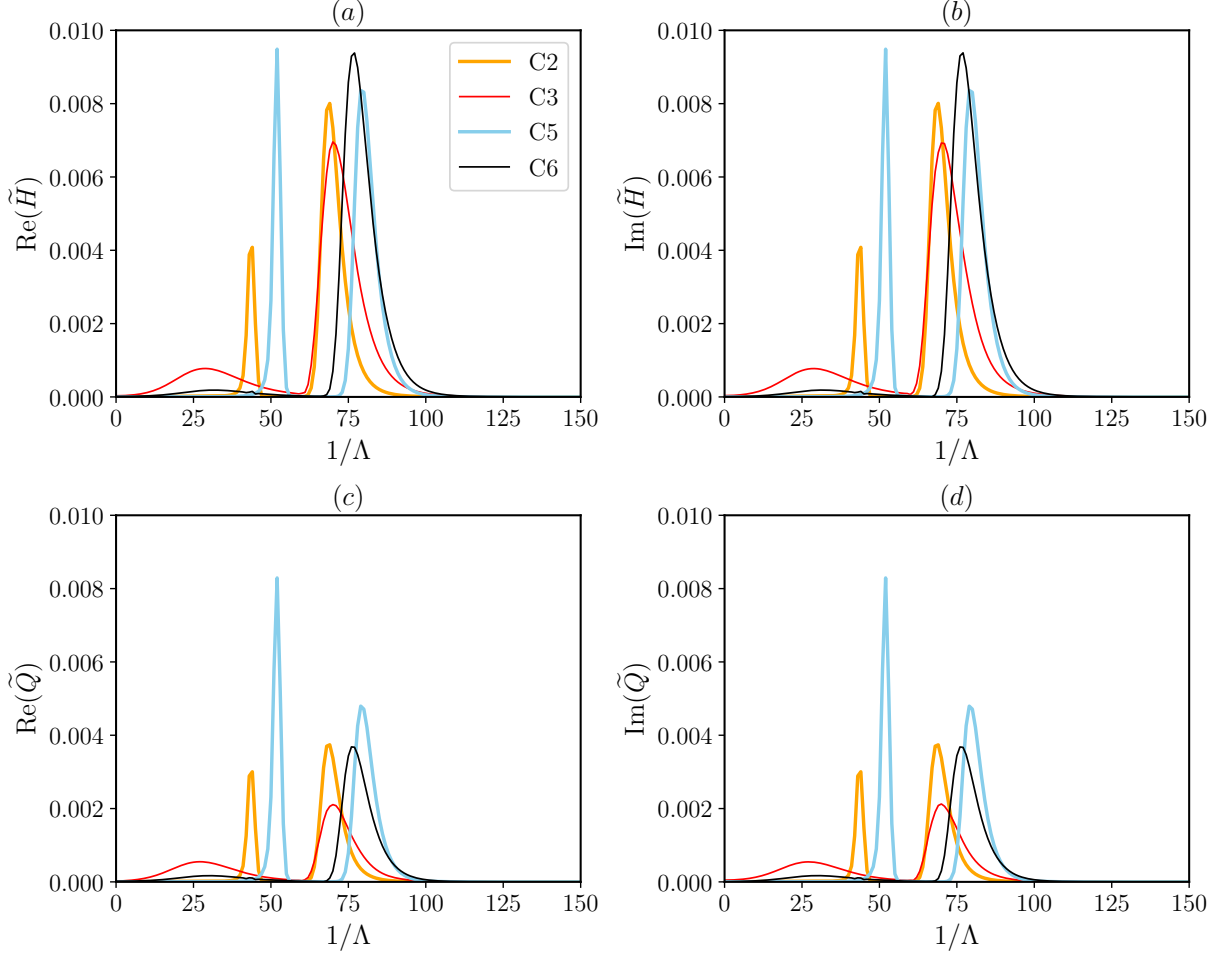


Figure 9: The spatial Fourier transform of the eigenfunctions from figure 8. Case C3 is scaled up by a factor of 10, while case C6 is scaled up a factor of 4.

is used for the time integration; see [the supplementary materials](#) for further details about the numerical method and its benchmarking.

### 8.1 Evolution from a perturbed inflated state

First, to validate the linear stability results from section 7, at  $T = 0$ , we perturb the steady-state solution of the 1D FSI model using the eigenfunction of a specific mode. Then,  $\text{Im}(\omega_G)$  indicates the decay/growth rate of the perturbation, while  $2\pi/\text{Re}(\omega_G)$  is the period of the perturbation's oscillations.

The first example is the linearly stable case C1 ( $q = 1500$   $\mu\text{l}/\text{min}$ ) perturbed from the steady state with the eigenfunctions of the pure decay modes tabulated in table 7. The shapes of the corresponding eigenfunctions are shown in figure 7. The decay rate of the perturbation to the steady flow agrees well with the corresponding  $\text{Im}(\omega_G)$ , as shown in figure 10(a). No oscillations are observed in the evolution of the perturbations because  $\text{Re}(\omega_G) = 0$  in this case.

The second example corresponds to the linearly unstable case C3. At  $T = 0$ , the steady state is perturbed at by the eigenfunction of the corresponding most unstable mode. The shape of the eigenfunctions are shown in figure 8, while the corresponding eigenvalues are given in table 7. Both the simulated growth rate and the oscillation period agree well with the linear stability analysis, as shown in figure 10(b). Here, note that the tension coefficient  $\theta_t$  in equation (4.12) is estimated from the instantaneous wall deformation, thus it is time dependent. Meanwhile  $\theta_t$  is fixed to be the steady-state value for the purposes of the linear stability

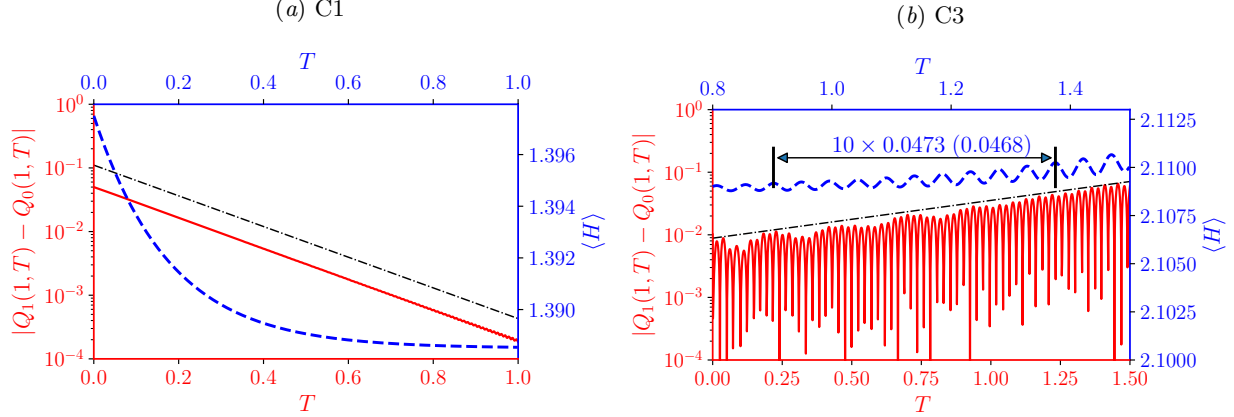


Figure 10: Time history of the difference between the instantaneous outlet flow rate and the steady one, *i.e.*,  $|Q(1, T) - Q_0(1, T)|$  (solid, left axes), and the axially average deformed height,  $\langle H \rangle = \int_0^1 \bar{H} dZ$  (dashed, right axes). (a) The steady state is perturbed using the eigenfunctions of the pure decay modes of case C1. (b) The steady state is perturbed using the eigenfunctions of the most unstable modes of case C3. The dot-dashed trendlines represent the growth/decay of perturbations, based on the imaginary part of the eigenvalues from table 7. In panel (b), the computed period of oscillation is marked. The value in parenthesis is from linear stability analysis, *i.e.*,  $2\pi/\text{Re}(\omega_G)$ .

analysis. The good agreement between the numerical simulation and the linear stability analysis indicates that neglecting the time dependence of  $\theta_t$  for the linear stability analysis is valid. The actual simulations for each case are conducted for a longer time window. Interestingly, although the oscillations of the system are sustained, no saturated periodic state emerges during the course of the simulation. The simulations cases C3 and C5 are available in appendix A.

## 8.2 Evolution from a flat initial state

Starting the simulations with an undeformed channel initial condition (as in equation (5.6)) would be more realistic of how a microfluidic device might be operated. With equation (5.6) as the initial condition, cases C1 and C4 are linearly stable and reach the steady state without detectable oscillations. The evolution of the representative quantities for case C4 are shown in figure 2 in the supplementary materials, while a video of the evolution under case C1 is provided in the supplementary materials. In this subsection, we focus on the two linearly unstable cases C3 and C6. All of the results shown below have been verified by time step refinement (see the supplementary materials and figure 3, for example).

First, the evolution of the outlet flow rate and the inlet pressure for cases C3 and C6 are shown in figure 11. In both cases, the outlet flow rate first decreases and then increases, reaching a value close to the imposed flow rate at late times. Meanwhile, the inlet pressure increases to a value slightly below the steady-state inlet pressure. Small-amplitude oscillations are observed in the evolution of both quantities. More importantly, the oscillations become magnified in at later times in the simulation, which suggests that these unstable cases will not reach the steady state. It can be shown (by running longer-time simulations) that these oscillations are not unbounded. Nevertheless, similar to the cases discussed in section 8.1, no saturated periodic state appears to emerge during the time window of the simulations shown in this subsection.

It is more enlightening to contrast the two simulations shown in figure 11. For these two cases, all system parameters are the same, except that the Young's modulus for case C3 is half of that for case C6. With a more compliant wall, the instabilities under case C3 develop more quickly. Specifically, more “violent” oscillations are observed in case C3 for the outlet flow rate and the inlet pressure than in case C6. These oscillation amplitudes could be, qualitatively, representative of the observations in dye-stream experiments. In other words, dye breakup could be expected when more violent oscillations occur in softer channels, while the dye stream may just oscillate (without breaking up) if the channel is less compliant (thus, the oscillations

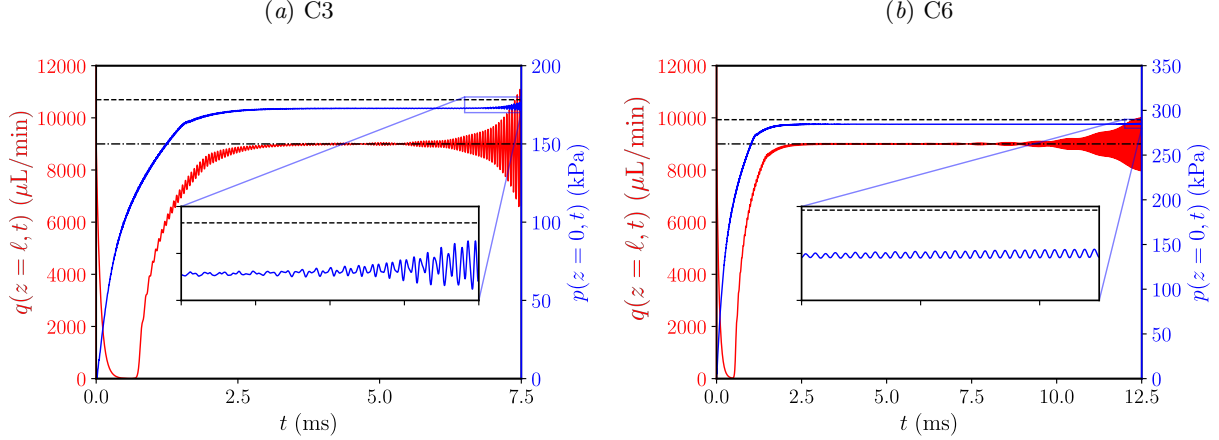


Figure 11: Time histories of the outlet flow rate and the inlet pressure for (a) case C3 and (b) case C6, respectively, with equation (5.6) being the initial condition. The dot-dashed lines mark the flow rate at steady state, while the dashed lines mark the inlet pressure at the steady state.

in the flow rate and pressure are milder). Indeed, it was observed in the experiments that the dye breaks up at lower  $Re$  in softer channels (Verma and Kumaran, 2013).

Next, let us take a closer look at the evolution of the fluid–solid interface. The example in figure 12 corresponds to case C3 in figure 11 (a), while the evolution under case C6 is qualitatively similar. Initially, for  $0 \leq t \leq 1$  ms as shown in figure 12(a), the interface bulges near the channel inlet first because the pressure is relatively high there. At the same time, transverse waves are shed and propagate from the inlet to the outlet until they are reflected at the downstream boundary of the domain. There is a dramatic increase in the total volume of fluid in the channel at this stage. Thereafter, the deformation of the wall stops growing, but the transverse waves still propagate back and forth along the fluid–solid interface. Compared with figure 12(a), the transverse waves have smaller wave length and amplitudes. Furthermore, the interface shape at this stage is close to the steady-state shape, as seen in figure 12(b). The deviation of the interface’s dynamic deformation from the steady one is plotted for  $4.0 \text{ ms} \leq t \leq 6.5 \text{ ms}$  in figure 12(c), where the wave propagation can be clearly observed. Interestingly, after a while, the oscillations near the channel’s outlet continue to grow and become larger than the oscillations anywhere else along the channel, which explains why the variations of the outlet flow rate appear more prominent compared than that of the inlet pressure in figure 11. This observation is also corroborated by the experimental observation that the instabilities always initiate near the channel’s outlet.

To better emphasize the difference in the wall motions near the inlet versus near the outlet, the vertical velocities of the fluid–solid interface at  $z = 0.9\ell$  (near the outlet) and  $z = 0.1\ell$  (near the inlet) of case C3 are plotted in figures 13 (see the supplementary materials for the details of reconstructing the velocities). The three stages discussed in figure 12 can also be identified from the time histories of the vertical velocities shown in these two figures. At early times, since the wall bulges first near the channel inlet, the vertical velocity at  $z = 0.1\ell$  is larger. The motion at  $z = 0.9\ell$  starts after the transverse waves reach the channel outlet. In the intermediate stage, during which the channel volume does not change significantly, the oscillations at both positions remain relatively small, until the motion near the outlet becomes amplified and leads to a striking difference in the oscillatory amplitudes at the two positions.

Figures 13(b) shows the corresponding time histories in the frequency (Fourier) domain. We observe that the peak is near the natural frequency of the wall (predicted by equation (7.8)), indicating a resonant phenomenon. Due to the FSI, which gives rise to the transverse waves along the fluid–solid interface, the pressure oscillations exhibit a frequency close to the natural frequency of the wall as well, causing a feedback. Note that, the resonances are *self-excited* as no oscillatory components are introduced in the initial condition (5.6). Further, the oscillations are self-sustained as they do not die out during the entire simulation time window. Consequently, the demonstrated FSI-induced instabilities could be an effective and inexpensive way of enhancing mixing at the microscale.

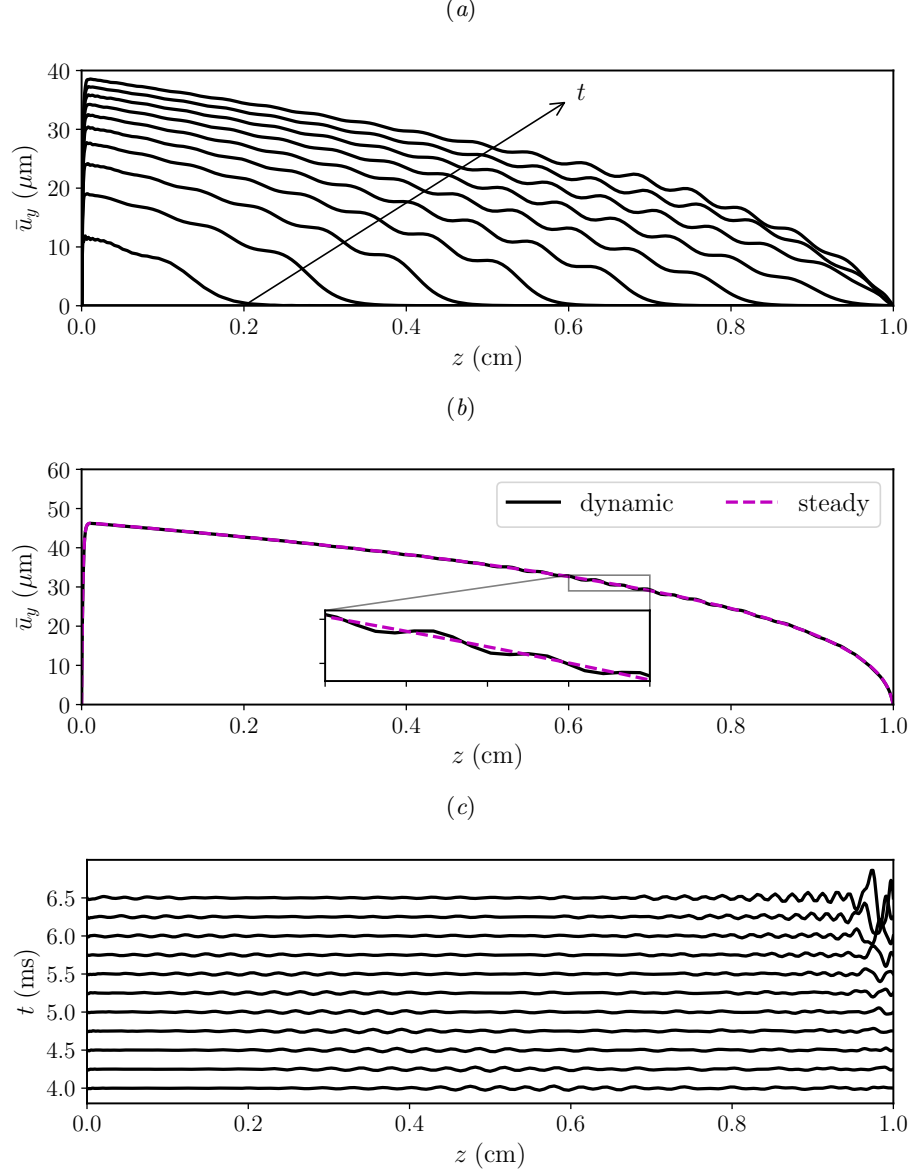


Figure 12: Evolution of the shape of the fluid–solid interface from the flat initial condition (5.6) (movie available in [the supplementary materials](#)). (a) Shape of the interface for  $0 \leq t \leq 1$  ms. (b) Comparison of the interface shape at  $t = 3.5$  ms with the steady state. (c) Difference between the instantaneous interface shape  $\bar{u}_y$  and the steady state  $\bar{u}_y^s$ , *i.e.*,  $\bar{u}_y - \bar{u}_y^s$ , for  $4.0 \text{ ms} \leq t \leq 6.5$  ms.

## 9 Conclusion

We derived a new 1D (reduced) FSI model for the physics underlying FSI-induced instabilities of flows conveyed in long and shallow microchannels with a deformable top wall. The key advance in our 1D FSI model, compared to previous work, lies in the accurate modeling of the wall deformation due to two-way FSI. For collapsible tubes, a constant large tension is always included, though bending was also considered in some computational studies (Luo et al., 2008; Liu et al., 2012; Wang et al., 2021). Similarly, the 1D FSI model of Inamdar et al. (2020) considered the top wall as a beam and took large-deformation-induced tension and bending into account. However, in a typical long and shallow rectangular microchannel, previous studies have demonstrated that, under linear elasticity, at the leading order, the soft wall deforms more like



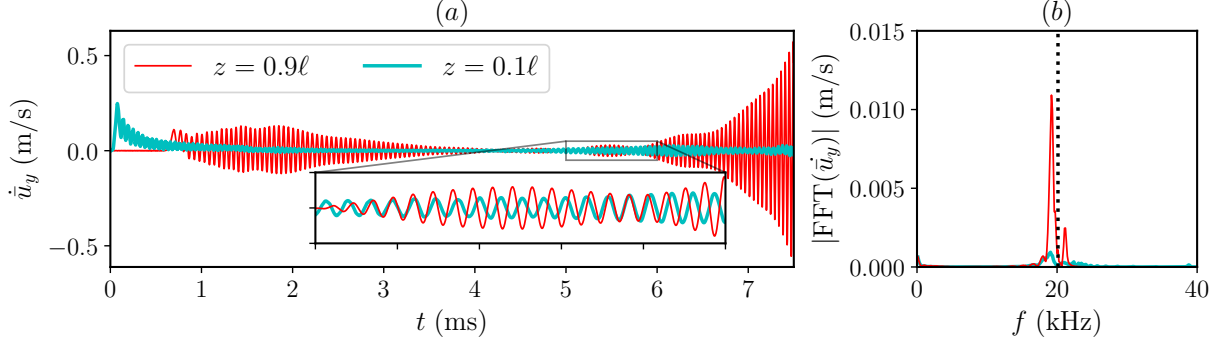


Figure 13: (a) Time histories of the vertical velocity of the fluid–solid interface of case C3 at  $z = 0.9\ell$  (near the outlet) and  $z = 0.1\ell$  (near the inlet), respectively. (b) Fourier transform of the corresponding time histories from (a). The dotted line marks the natural frequency calculated from equation (7.8).

a Winkler foundation, *i.e.*, the deformation of the channel’s cross-section at different streamwise locations is fully determined by the local pressure (Christov et al., 2018; Shidhore and Christov, 2018; Wang and Christov, 2019). Hence, in contrast to other 1D models, the 1D FSI model proposed herein maintains the dominance of the Winkler-foundation-like behavior of the soft wall. Weak tension was introduced only to take account into the boundary effects near the inlet and outlet of the channel. Moreover, the inertia of the solid was also modelled consistently, just like the inertia of the fluid was take into account by lubrication theory at low, but finite, Reynolds number, following (Wang and Christov, 2021). Our proposed 1D model establishes how the unsteady flow rate, the pressure and the channel deformation evolve together in a tightly coupled manner.

Importantly, we found that the predictions of the proposed 1D FSI model agree qualitatively with key experiments (Verma and Kumaran, 2013) (summarized in table 6). Consequently, we believe that the present analysis leads to significant, novel insight into the experimentally observed low- $Re$  FSI-induced instabilities in compliant microchannels. In short, the physical insight provided by our new model is that FSI causes wall resonances, giving rise to self-sustained oscillations of the fluid–solid interface. These resonance occur in a regime of weak axial tension and require finite solid inertia. Further, the experimentally observed dye breakup (and “ultrafast” mixing) are explained by the global instability of non-flat (deformed) base state of our model, which was not accurately accounted for in previous work. Our proposed 1D FSI model allows for the identification (computationally) of the critical conditions for instability of this coupled system. The predicted critical Reynolds number is in agreement with the value suggested by experiments.

To the experimentalist, our proposed 1D FSI model provides a tool through which different microchannel designs can be rapidly prototyped and evaluated. Beyond that, our model provides a convenient way to evaluate operating conditions that might lead to instability and mixing. Extending the present results, the pressure drop could be prescribed across the channel (instead of fixing the flux at the inlet), similarly to the works of Stewart et al. (2009, 2010). Further, the proposed 1D modeling framework can be easily used to analyze soft conduits of different cross-sectional geometries and other boundary conditions, as long as the basic assumptions on the separation of scales (and weak versus dominant effects in the solid) are not violated.

The current work was motivated by microfluidic experiments and aimed to provide new qualitative and quantitative physical insights into the phenomena. Nevertheless, further work is needed to understand the full range of dynamic behaviors possible under the proposed 1D FSI model. For example, in the linearly unstable case, the numerical simulations of the model using different time step sizes begin to diverge after a certain (long) integration time. This observation reminds us of the similarly chaotic behavior observed in a 1D FSI model derived by Jensen (1992) in the somewhat different context of collapsible tubes. Similar to our 1D FSI model, Jensen’s model also exhibits multiple unstable modes, and its dynamics may be sensitive to initial conditions (due to the interactions of multiple unstable modes). Therefore, understanding the nonlinear dynamics of the proposed 1D FSI model could be a fruitful avenue for future work. Further, since the observed oscillations are low-amplitude and high-frequency, asymptotic analysis could yield the stability

boundaries (Jensen and Heil, 2003). On the other hand, an Orr–Sommerfeld-type local stability analysis (similarly to the Kumaran family of studies, recall section 1) could once again be conducted on the proposed model to complement to the global stability analysis. Investigating the connections between the local and global instabilities could provide insight regarding what types of excitations trigger unstable global modes (Stewart et al., 2009, 2010), opening the door towards more controllable “ultrafast mixing” due to FSIs in compliant microchannels.

## Acknowledgements

This work originates from research partially supported by the US National Science Foundation under grant No. CBET-1705637. We thank E. Boyko for feedback on an earlier draft.

## Appendix A Long-time simulation of the evolution from a perturbed inflated state

The linear stability analysis only predicts the evolution of the perturbation in the vicinity of the steady state, *i.e.*, for early times. The simulations in section 8.1 are actually conducted for a longer time window. The results for cases C3 and C5 are shown in figures 14 and 15, respectively. For the time window shown, the numerical results are verified by time step refinement. All representative quantities shown in figures 14 and 15 experience high-frequency oscillations with nonlinear variations in their amplitudes. No saturated (periodic) state is found in any of the cases. Actually, beyond the given time window, the simulation results diverge when using different time step sizes, which suggests that this nonlinear dynamical system may exhibit chaotic behavior. However, pursuing this possibility is beyond the scope of the present work. The most important conclusion from these simulations is that the perturbed steady state is unstable, and the system undergoes self-sustained oscillations, instead of returning to the inflated steady state.

In figure 14 and figure 15, the axially averaged deformed height (first rows), the inlet pressure and the axially averaged pressure (second rows) are observed to vary in a small range ( $< 1 \mu\text{m}$  for the axially averaged deformation and  $< 10 \text{ kPa}$  for the pressure), which is consistent with the fact that no dramatic changes in the channel volume and the inlet pressure were reported in the experiments (Verma and Kumaran, 2013). On the contrary, the outlet flow rate (third rows) experiences more violent oscillations, which are prominent near the channel outlet, as shown in figure 8. In the fourth rows, the vertical velocity of the fluid–solid interface is shown. It is obtained based via equation (5.1) and conservation of mass (see the supplementary materials for further details). Like the flow rate, the vertical velocity of the interface is observed to experience larger oscillatory amplitude near the channel outlet than that near the channel inlet, which again matches the experimental observation that the instabilities initiate near the channel’s outlet.

Figures 14(b) and 15(b) show the Fourier transform of the time history of the corresponding representative quantity. It is observed that there is a peak near  $f_g$  (see equation (7.7)), showing a good agreement with the linear stability analysis. Also observe that  $f_g$  is close to the natural frequency of the wall,  $f_n$  (see equation (7.8)), which indicates that the wall oscillations are a resonance phenomenon. Further, nonlinearity generates higher harmonics. In figure 14, there is another peak at  $\approx 2f_g$ , while in figure 15, the second peak is at a frequency higher than  $2f_g$ . The higher-frequency oscillations are more prominent near the channel inlet. For example, the second peak of the vertical velocity of the interface at  $z = 0.1 \text{ cm}$  is taller than the first peak. Furthermore, the higher-frequency oscillations in the inlet pressure are more prominent than the lower-frequency oscillations as shown in both figures 14 and 15.

## References

- Anand, V., Muchandimath, S.C., Christov, I.C., 2020. Hydrodynamic Bulge Testing: Materials Characterization Without Measuring Deformation. *ASME J. Appl. Mech.* 87, 051012. doi:[10.1115/1.4046297](https://doi.org/10.1115/1.4046297).
- Boyd, J.P., 2000. Chebyshev and Fourier Spectral Methods. 2 ed., Dover Publications, Mineola, NY.
- Christov, I.C., 2022. Soft hydraulics: from Newtonian to complex fluid flows through compliant conduits. *J. Phys.: Condens. Matter* 34, 063001. doi:[10.1088/1361-648X/ac327d](https://doi.org/10.1088/1361-648X/ac327d).

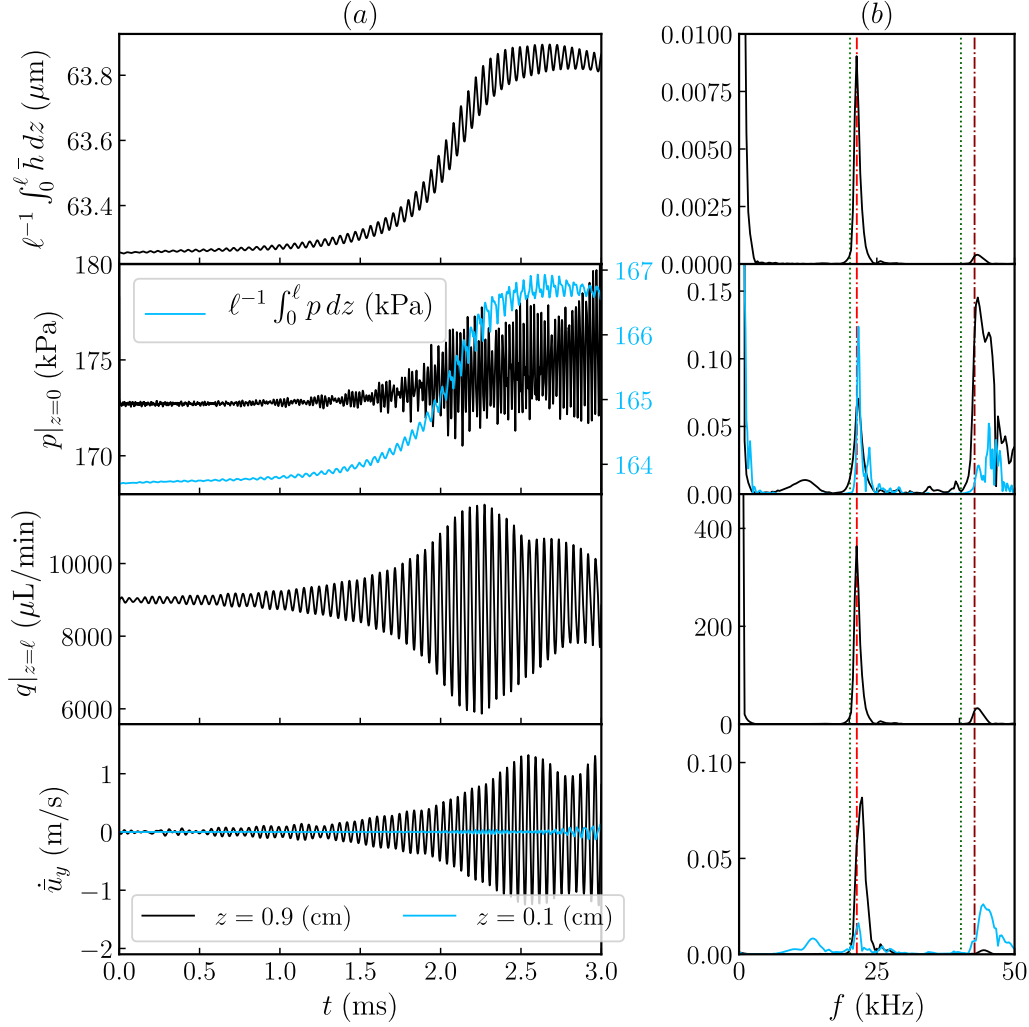


Figure 14: Dynamic simulations of case C3, by perturbing the steady state with the eigenfunctions of the most unstable mode from table 7. (a) Time histories of representative quantities: the axially averaged deformed height, the inlet pressure and the axially averaged pressure, the outlet flow rate, and the vertical velocity of the interface at  $z = 0.9$  cm and  $z = 0.1$  cm, respectively, from top to below. (b) Fourier transform of the time signals from (a). Note that in the second and fourth rows, the vertical axis has been scaled for a clearer view. The dot-dashed lines mark  $f_g$  and  $2f_g$  (see equation (7.7)), while the dotted lines mark  $f_n$  and  $2f_n$  (see equation (7.8)).

Christov, I.C., Cognet, V., Shidhore, T.C., Stone, H.A., 2018. Flow rate–pressure drop relation for deformable shallow microfluidic channels. *J. Fluid Mech.* 814, 267–286. doi:[10.1017/jfm.2018.30](https://doi.org/10.1017/jfm.2018.30).

Dhong, C., Edmunds, S.J., Ramírez, J., Kayser, L.V., Chen, F., Jokerst, J.V., Lipomi, D.J., 2018. Optics-free, non-contact measurements of fluids, bubbles, and particles in microchannels using metallic nano-islands on graphene. *Nano Lett.* 18, 5306–5311. doi:[10.1021/acs.nanolett.8b02292](https://doi.org/10.1021/acs.nanolett.8b02292).

Di Carlo, D., Irimia, D., Tompkins, R.G., Toner, M., 2007. Continuous inertial focusing, ordering, and separation of particles in microchannels. *Proc. Natl Acad. Sci. USA* 104, 18892–18897. doi:[10.1073/pnas.0704958104](https://doi.org/10.1073/pnas.0704958104).

Dillard, D.A., Mukherjee, B., Karnal, P., Batra, R.C., Frechette, J., 2018. A review of Winkler’s foundation and its profound influence on adhesion and soft matter applications. *Soft Matter* 14, 3669–3683. doi:[10.1039/c7sm02062g](https://doi.org/10.1039/c7sm02062g).

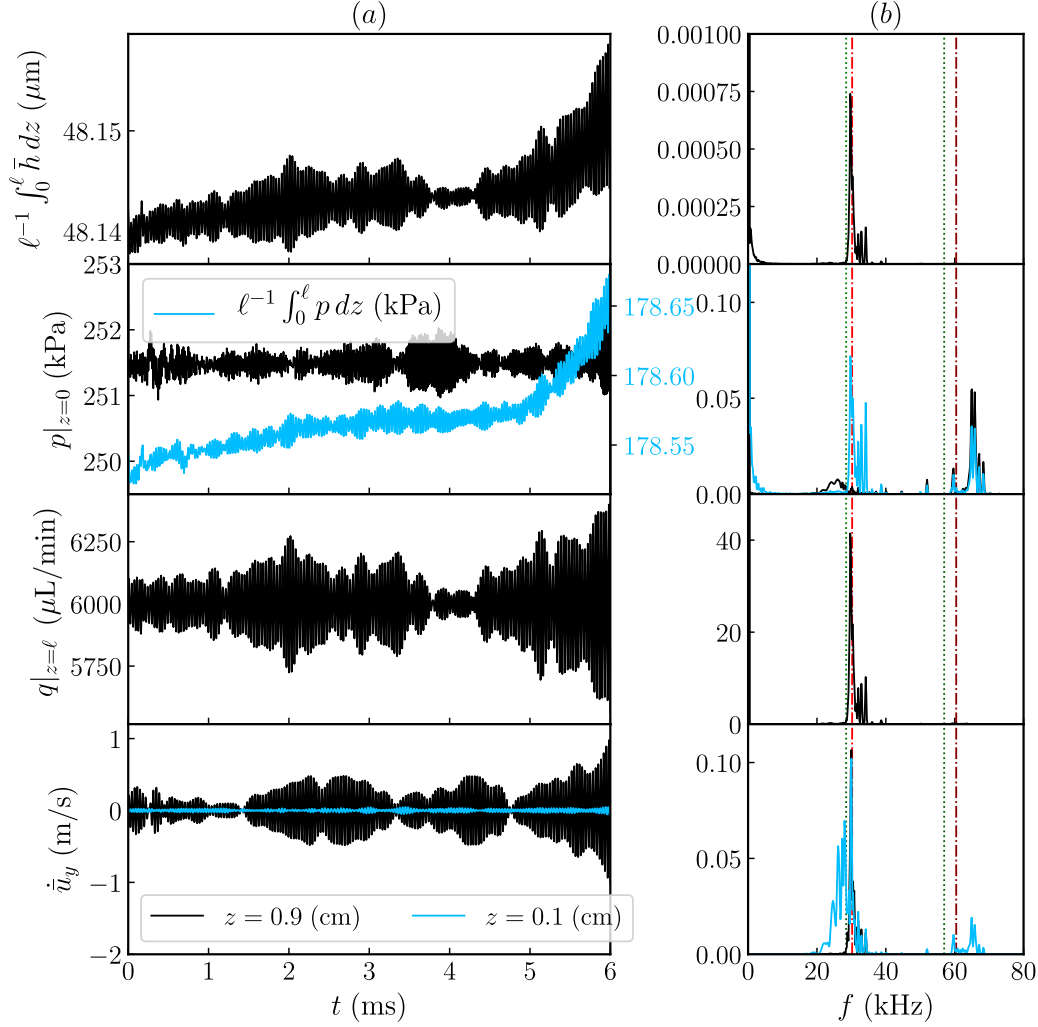


Figure 15: Dynamic simulations of case C5, by perturbing the steady state with the eigenfunctions of the most unstable mode from table 7. (a) Time histories of the representative quantities: the axially averaged deformed height, the inlet pressure and the axially averaged pressure, the outlet flow rate, and the vertical velocity of the interface at  $z = 0.9$  cm and  $z = 0.1$  cm, respectively, from top to below. (b) Fourier transform of the time signals from (a). Note that in the second and fourth rows, the vertical axis has been scaled to highlight the smaller-scale details. The dot-dashed lines mark  $f_g$  and  $2f_g$  (see equation (7.7)), while the dotted lines mark  $f_n$  and  $2f_n$  (see equation (7.8)).

- Elbaz, S.B., Gat, A.D., 2014. Dynamics of viscous liquid within a closed elastic cylinder subject to external forces with application to soft robotics. *J. Fluid Mech.* 758, 221–237. doi:[10.1017/jfm.2014.527](https://doi.org/10.1017/jfm.2014.527).
- Gaurav, Shankar, V., 2009. Stability of fluid flow through deformable neo-Hookean tubes. *J. Fluid Mech.* 627, 291–322. doi:[10.1017/S0022112009005928](https://doi.org/10.1017/S0022112009005928).
- Gervais, T., El-Ali, J., Günther, A., Jensen, K.F., 2006. Flow-induced deformation of shallow microfluidic channels. *Lab Chip* 6, 500–507. doi:[10.1039/b513524a](https://doi.org/10.1039/b513524a).
- Gkanis, V., Kumar, S., 2005. Stability of pressure-driven creeping flows in channels lined with a nonlinear elastic solid. *J. Fluid Mech.* 524, 357–375. doi:[10.1017/S0022112004002472](https://doi.org/10.1017/S0022112004002472).
- Gad-el Hak, M., 2002. Compliant coatings for drag reduction. *Prog. Aerospace Sci.* 38, 77–99. doi:[10.1016/S0376-0421\(01\)00020-3](https://doi.org/10.1016/S0376-0421(01)00020-3).

- Heil, M., Boyle, J., 2010. Self-excited oscillations in three-dimensional collapsible tubes: simulating their onset and large-amplitude oscillations. *J. Fluid Mech.* 652, 405–426. doi:[10.1017/S0022112010000157](https://doi.org/10.1017/S0022112010000157).
- Hewitt, I.J., Balmforth, N.J., De Bruyn, J.R., 2015. Elastic-plated gravity currents. *Eur. J. Appl. Math.* 26, 1–31. doi:[10.1017/S0956792514000291](https://doi.org/10.1017/S0956792514000291).
- Hosokawa, K., Hanada, K., Maeda, R., 2002. A polydimethylsiloxane (PDMS) deformable diffraction grating for monitoring of local pressure in microfluidic devices. *J. Microelectromechan. Syst.* 12, 1–6. doi:[10.1088/0960-1317/12/1/301](https://doi.org/10.1088/0960-1317/12/1/301).
- Huerre, P., Monkewitz, P.A., 1990. Local and Global Instabilities in Spatially Developing Flows. *Annu. Rev. Fluid Mech.* 22, 473–537. doi:[10.1146/annurev.fl.22.010190.002353](https://doi.org/10.1146/annurev.fl.22.010190.002353).
- Inamdar, T.C., Wang, X., Christov, I.C., 2020. Unsteady fluid-structure interactions in a soft-walled microchannel: A one-dimensional lubrication model for finite Reynolds number. *Phys. Rev. Fluids* 5, 064101. doi:[10.1103/PhysRevFluids.5.064101](https://doi.org/10.1103/PhysRevFluids.5.064101).
- Jensen, O.E., 1990. Instabilities of flow in a collapsed tube. *J. Fluid Mech.* 220, 623–659. doi:[10.1017/S0022112090003408](https://doi.org/10.1017/S0022112090003408).
- Jensen, O.E., 1992. Chaotic Oscillations in a Simple Collapsible-Tube Model. *ASME J. Biomech. Eng.* 114, 55–59. doi:[10.1115/1.2895450](https://doi.org/10.1115/1.2895450).
- Jensen, O.E., Heil, M., 2003. High-frequency self-excited oscillations in a collapsible-channel flow. *J. Fluid Mech.* 481, 235–268. doi:[10.1017/S002211200300394X](https://doi.org/10.1017/S002211200300394X).
- Jensen, O.E., Pedley, T.J., 1989. The existence of steady flow in a collapsed tube. *J. Fluid Mech.* 206, 339–374. doi:[10.1017/S0022112089002326](https://doi.org/10.1017/S0022112089002326).
- Karan, P., Chakraborty, J., Chakraborty, S., Wereley, S.T., Christov, I.C., 2021. Profiling a soft solid layer to passively control the conduit shape in a compliant microchannel during flow. *Phys. Rev. E* 104, 015108. doi:[10.1103/PhysRevE.104.015108](https://doi.org/10.1103/PhysRevE.104.015108).
- Karnik, R., 2013. Microfluidic Mixing, in: Li, D. (Ed.), *Encyclopedia of Microfluidics and Nanofluidics*. Springer, Boston, MA, pp. 1–13. doi:[10.1007/978-3-642-27758-0\\_{\\\_}939-2](https://doi.org/10.1007/978-3-642-27758-0_{\_}939-2).
- Keller, H.B., 1976. Numerical Solution of Two Point Boundary Value Problems. volume 24 of *CBMS-NSF Regional Conference Series in Applied Mathematics*. SIAM, Philadelphia, PA. doi:[10.1137/1.9781611970449](https://doi.org/10.1137/1.9781611970449).
- Krindel, P., Silberberg, A., 1979. Flow through gel-walled tubes. *J. Colloid Interface Sci.* 71, 39–50. doi:[10.1016/0021-9797\(79\)90219-4](https://doi.org/10.1016/0021-9797(79)90219-4).
- Kumaran, V., 1995. Stability of the viscous flow of a fluid through a flexible tube. *J. Fluid Mech.* 294, 259–281. doi:[10.1017/S0022112095002886](https://doi.org/10.1017/S0022112095002886).
- Kumaran, V., 2021. Stability and the transition to turbulence in the flow through conduits with compliant walls. *J. Fluid Mech.* 924, P1. doi:[10.1017/jfm.2021.602](https://doi.org/10.1017/jfm.2021.602).
- Kumaran, V., Bandaru, P., 2016. Ultra-fast microfluidic mixing by soft-wall turbulence. *Chem. Eng. Sci.* 149, 156–168. doi:[10.1016/j.ces.2016.04.001](https://doi.org/10.1016/j.ces.2016.04.001).
- Liu, H.F., Luo, X.Y., Cai, Z.X., 2012. Stability and energy budget of pressure-driven collapsible channel flows. *J. Fluid Mech.* 705, 348–370. doi:[10.1017/jfm.2011.254](https://doi.org/10.1017/jfm.2011.254).
- Love, A.E.H., 1888. The small free vibrations and deformation of a thin elastic shell. *Phil. Trans. R. Soc. Lond. A* 179, 491–546. doi:[10.1098/rsta.1888.0016](https://doi.org/10.1098/rsta.1888.0016).
- Luo, X.Y., Cai, Z.X., Li, W.G., Pedley, T.J., 2008. The cascade structure of linear instability in collapsible channel flows. *J. Fluid Mech.* 600, 45–76. doi:[10.1017/S0022112008000293](https://doi.org/10.1017/S0022112008000293).
- Luo, X.Y., Pedley, T.J., 1996. A numerical simulation of unsteady flow in a two-dimensional collapsible channel. *J. Fluid Mech.* 314, 191–225. doi:[10.1017/S0022112096000286](https://doi.org/10.1017/S0022112096000286).
- Luo, X.Y., Pedley, T.J., 1998. The effects of wall inertia on flow in a two-dimensional collapsible channel. *J. Fluid Mech.* 363, 253–280. doi:[10.1017/S0022112098001062](https://doi.org/10.1017/S0022112098001062).
- Martínez-Calvo, A., Sevilla, A., Peng, G.G., Stone, H.A., 2020. Start-up flow in shallow deformable microchannels. *J. Fluid Mech.* 885, A25. doi:[10.1017/jfm.2019.994](https://doi.org/10.1017/jfm.2019.994).
- Mindlin, R.D., 1951. Influence of rotatory inertia and shear on flexural motions of isotropic, elastic plates. *ASME J. Appl. Mech.* 18, 31–38.

- Neelamegam, R., Shankar, V., 2015. Experimental study of the instability of laminar flow in a tube with deformable walls. *Phys. Fluids* 27, 024102. doi:[10.1063/1.4907246](https://doi.org/10.1063/1.4907246).
- Ottino, J.M., Wiggins, S., 2004. Introduction: mixing in microfluidics. *Phil. Trans. R. Soc. A* 362, 923–935. doi:[10.1098/rsta.2003.1355](https://doi.org/10.1098/rsta.2003.1355).
- Ozsun, O., Yakhot, V., Ekinci, K.L., 2013. Non-invasive measurement of the pressure distribution in a deformable micro-channel. *J. Fluid Mech.* 734, R1. doi:[10.1017/jfm.2013.474](https://doi.org/10.1017/jfm.2013.474).
- Panton, R.L., 2013. *Incompressible Flow*. 4th ed., John Wiley & Sons, Hoboken, NJ. doi:[10.1002/9781118713075](https://doi.org/10.1002/9781118713075).
- Patne, R., Shankar, V., 2019. Stability of flow through deformable channels and tubes: implications of consistent formulation. *J. Fluid Mech.* 860, 837–885. doi:[10.1017/jfm.2018.908](https://doi.org/10.1017/jfm.2018.908).
- Peng, G.G., Lister, J.R., 2020. Viscous flow under an elastic sheet. *J. Fluid Mech.* 905, A30. doi:[10.1017/jfm.2020.745](https://doi.org/10.1017/jfm.2020.745).
- Pihler-Puzović, D., Pedley, T.J., 2014. Flutter in a quasi-one-dimensional model of a collapsible channel. *Proc. R. Soc. A* 470, 20140015. doi:[10.1098/rspa.2014.0015](https://doi.org/10.1098/rspa.2014.0015).
- Pohlhausen, K., 1921. Zur näherungsweise Integration der Differentialgleichung der laminaren Grenzschicht. *Z. Angew. Math. Mech. (ZAMM)* 1, 252–290. doi:[10.1002/zamm.19210010402](https://doi.org/10.1002/zamm.19210010402).
- Reissner, E., 1945. The effect of transverse shear deformation on the bending of elastic plates. *ASME J. Appl. Mech.* 12, A68–A77.
- Sackmann, E.K., Fulton, A.L., Beebe, D.J., 2014. The present and future role of microfluidics in biomedical research. *Nature* 507, 181–189. doi:[10.1038/nature13118](https://doi.org/10.1038/nature13118).
- Seker, E., Leslie, D.C., Haj-Hariri, H., Landers, J.P., Utz, M., Begley, M.R., 2009. Nonlinear pressure-flow relationships for passive microfluidic valves. *Lab Chip* 9, 2691–2697. doi:[10.1039/B903960K](https://doi.org/10.1039/B903960K).
- Shapiro, A.H., 1977. Steady flow in collapsible tubes. *ASME J. Biomech. Eng.* 99, 126–147. doi:[10.1115/1.3426281](https://doi.org/10.1115/1.3426281).
- Shen, J., Tang, T., Wang, L.L., 2011. *Spectral Methods: Algorithms, Analysis and Applications*. volume 41 of *Springer Series in Computational Mathematics*. Springer-Verlag, Berlin/Heidelberg. doi:[10.1007/978-3-540-71041-7](https://doi.org/10.1007/978-3-540-71041-7).
- Shiba, K., Li, G., Viot, E., Yoshikawa, G., Weitz, D.A., 2021. Microchannel measurements of viscosity for both gases and liquids. *Lab Chip* 21, 2805–2811. doi:[10.1039/D1LC00202C](https://doi.org/10.1039/D1LC00202C).
- Shidhore, T.C., Christov, I.C., 2018. Static response of deformable microchannels: a comparative modelling study. *J. Phys.: Condens. Matter* 30, 054002. doi:[10.1088/1361-648X/aaa226](https://doi.org/10.1088/1361-648X/aaa226).
- Srinivas, S.S., Kumaran, V., 2015. After transition in a soft-walled microchannel. *J. Fluid Mech.* 780, 649–686. doi:[10.1017/jfm.2015.476](https://doi.org/10.1017/jfm.2015.476).
- Srinivas, S.S., Kumaran, V., 2017. Transitions to different kinds of turbulence in a channel with soft walls. *J. Fluid Mech.* 822, 267–306. doi:[10.1017/jfm.2017.270](https://doi.org/10.1017/jfm.2017.270).
- Stewart, P., Foss, A.J.E., 2019. Self-excited oscillations in a collapsible channel with applications to retinal venous pulsation. *ANZIAM J.* 61, 320–348. doi:[10.1017/S1446181119000117](https://doi.org/10.1017/S1446181119000117).
- Stewart, P., Heil, M., Waters, S.L., Jensen, O.E., 2010. Sloshing and slamming oscillations in a collapsible channel flow. *J. Fluid Mech.* 662, 288–319. doi:[10.1017/S0022112010003277](https://doi.org/10.1017/S0022112010003277).
- Stewart, P.S., Waters, S.L., Jensen, O.E., 2009. Local and global instabilities of flow in a flexible-walled channel. *Eur. J. Mech. B/Fluids* 28, 541–557. doi:[10.1016/j.euromechflu.2009.03.002](https://doi.org/10.1016/j.euromechflu.2009.03.002).
- Subbaraj, K., Dokainish, M., 1989. A survey of direct time-integration methods in computational structural dynamics—II. Implicit methods. *Comput. Struct.* 32, 1387–1401. doi:[10.1016/0045-7949\(89\)90315-5](https://doi.org/10.1016/0045-7949(89)90315-5).
- Timoshenko, S., Woinowsky-Krieger, S., 1959. *Theory of Plates and Shells*. 2nd ed., McGraw-Hill, New York.
- Verma, M.K.S., Kumaran, V., 2012. A dynamical instability due to fluid-wall coupling lowers the transition Reynolds number in the flow through a flexible tube. *J. Fluid Mech.* 705, 322–347. doi:[10.1017/jfm.2011.55](https://doi.org/10.1017/jfm.2011.55).
- Verma, M.K.S., Kumaran, V., 2013. A multifold reduction in the transition Reynolds number, and ultra-fast mixing, in a micro-channel due to a dynamical instability induced by a soft wall. *J. Fluid Mech.* 727,



- 407–455. doi:[10.1017/jfm.2013.264](https://doi.org/10.1017/jfm.2013.264).
- Verma, M.K.S., Kumaran, V., 2015. Stability of the flow in a soft tube deformed due to an applied pressure gradient. *Phys. Rev. E* 91, 043001. doi:[10.1103/PhysRevE.91.043001](https://doi.org/10.1103/PhysRevE.91.043001).
- Virtanen, P., Gommers, R., Oliphant, T.E., Haberland, M., Reddy, T., Cournapeau, D., Burovski, E., Peterson, P., Weckesser, W., Bright, J., van der Walt, S.J., Brett, M., Wilson, J., Millman, K.J., Mayorov, N., Nelson, A.R.J., Jones, E., Kern, R., Larson, E., Carey, C.J., Polat, I., Feng, Y., Moore, E.W., VanderPlas, J., Laxalde, D., Perktold, J., Cimrman, R., Henriksen, I., Quintero, E.A., Harris, C.R., Archibald, A.M., Ribeiro, A.H., Pedregosa, F., van Mulbregt, P., 2020. SciPy 1.0: fundamental algorithms for scientific computing in Python. *Nature Methods* 17, 261–272. doi:[10.1038/s41592-019-0686-2](https://doi.org/10.1038/s41592-019-0686-2).
- Wang, D., Luo, X., Stewart, P., 2021. Energetics of collapsible channel flow with a nonlinear fluid-beam model. *J. Fluid Mech.* 926, A2. doi:[10.1017/jfm.2021.642](https://doi.org/10.1017/jfm.2021.642).
- Wang, X., Christov, I.C., 2019. Theory of the flow-induced deformation of shallow compliant microchannels with thick walls. *Proc. R. Soc. A* 475, 20190513. doi:[10.1098/rspa.2019.0513](https://doi.org/10.1098/rspa.2019.0513).
- Wang, X., Christov, I.C., 2020. Soft hydraulics in channels with thick walls: The finite-Reynolds-number base state and its stability, in: Todorov, M.D. (Ed.), *Proceedings of the 12th International On-line Conference for Promoting the Application of Mathematics in Technical and Natural Sciences - AMiTaN'S'20*. AIP, volume 2302 of *AIP Conference Proceedings*, p. 020002. doi:[10.1063/5.0033517](https://doi.org/10.1063/5.0033517).
- Wang, X., Christov, I.C., 2021. Reduced models of unidirectional flows in compliant rectangular ducts at finite Reynolds number. *Phys. Fluids* 33, 102004. doi:[10.1063/5.0062252](https://doi.org/10.1063/5.0062252).
- White, F.M., 2006. *Viscous Fluid Flow*. 3 ed., McGraw-Hill Higher Education, New York, NY.
- Winkler, E., 1867. *Die Lehre von der Elastizität und Festigkeit mit besonderer Rücksicht auf ihre Anwendung in der Technik*. Verlag von H. Dominicus, Prag. URL: [https://www.google.com/books/edition/\\_/25E5AAAAcAAJ](https://www.google.com/books/edition/_/25E5AAAAcAAJ).
- Xu, F., Billingham, J., Jensen, O.E., 2013. Divergence-driven oscillations in a flexible-channel flow with fixed upstream flux. *J. Fluid Mech.* 723, 706–733. doi:[10.1017/jfm.2013.97](https://doi.org/10.1017/jfm.2013.97).
- Xu, F., Billingham, J., Jensen, O.E., 2014. Resonance-driven oscillations in a flexible-channel flow with fixed upstream flux and a long downstream rigid segment. *J. Fluid Mech.* 746, 368–404. doi:[10.1017/jfm.2014.136](https://doi.org/10.1017/jfm.2014.136).

# Supplementary Materials

## Reduced modeling and global instability of finite-Reynolds-number flow in compliant rectangular channels

Xiaojia Wang, Ivan C. Christov

*School of Mechanical Engineering, Purdue University, West Lafayette, Indiana, 47907, USA*

February 24, 2022

### SM.1 Numerical scheme for the 1D FSI model

Here, we introduce a numerical scheme used for solving the coupled problem of deformation-induced tension, wall deformation, and flow. This scheme is also applied to the simpler case of constant tension with given  $\theta_t$ . The spatial domain is discretized using the pseudospectral method (Boyd, 2000), with which the governing equations are satisfied at preassigned Gauss-type-quadrature nodes. In our case, the Gauss–Lobatto points are chosen. Therefore, the method is also referred to as “Chebyshev pseudospectral method” or “Chebyshev collocation method.” Note that in some literature (Shen et al., 2011), the pseudospectral method is specifically referred to as a Galerkin-type method with the numerical integration using a Gauss-type quadrature, which is not the case for the present method.

The Gauss–Lobatto points

$$\tilde{Z}_j = -\cos\left(\frac{j\pi}{N}\right), \quad j = 0, 1, \dots, N \quad (\text{SM.1.1})$$

are defined on the domain  $[-1, 1]$ . (Note that  $\tilde{Z}_0 = -1$  and  $\tilde{Z}_N = 1$ .) Consequently, we use a change of variables,  $\tilde{Z} = 2Z - 1$ , to transform the computational domain from  $\{Z | Z \in [0, 1]\}$  to  $\{\tilde{Z} | \tilde{Z} \in [-1, 1]\}$ . Then,  $d^m/dZ^m = 2^m d^m/d\tilde{Z}^m$ . There are two major advantages of choosing the Gauss–Lobatto points as the collocation points. First, the Gauss–Lobatto points are nonuniformly distributed and clustered near the endpoints  $\tilde{Z} = \pm 1$ , with the spacing scaling as  $\mathcal{O}(N^{-2})$ , which helps resolve the deformation boundary layer near the channel outlet. Second, it is convenient to compute derivatives at the Gauss–Lobatto points. Essentially, the Chebyshev pseudospectral method finds a high-order polynomial-based, valid in the whole domain, to approximate the actual solution. As long as the functional values are known at the  $N + 1$  collocated points, an  $N$ -order polynomial can be uniquely determined.

The Lagrange basis,  $l_j(Z)$  ( $j = 0, 1, \dots, N$ ), is a convenient choice for the interpolating polynomial since the coefficients are just the functional values. Here,  $l_j$  denotes the Lagrange polynomial which takes the value of 1 at  $\tilde{Z} = Z_j$  while being 0 for  $Z_k$  with  $k \neq j$ . Importantly, the derivatives of the Lagrange basis at the Gauss–Lobatto points are known analytically. For example, taking  $Q_k \approx Q|_{\tilde{Z}=\tilde{Z}_k}$ ,  $k = 0, 1, \dots, N$ , then

$dQ/d\tilde{Z}|_{\tilde{Z}=\tilde{Z}_k} \approx \sum_{j=0}^N D_{kj}^{(1)} Q_j$ . Here, the components of the first-order differentiation matrix  $\mathbf{D}^{(1)}$  are:

$$D_{kj}^{(1)} = \left. \frac{dl_j}{d\tilde{Z}} \right|_{\tilde{Z}=\tilde{Z}_k} = \begin{cases} -\frac{2N^2+1}{6}, & k=j=0, \\ \frac{\tilde{c}_k}{\tilde{c}_j} \frac{(-1)^{k+j}}{\tilde{Z}_k - \tilde{Z}_j}, & k \neq j, \quad 0 \leq k, j \leq N, \\ -\frac{\tilde{Z}_k}{2(1-\tilde{Z}_k^2)}, & k=j, \quad 1 \leq k, j \leq N-1, \\ \frac{2N^2+1}{6}, & k=j=N, \end{cases} \quad (\text{SM.1.2})$$

where  $\tilde{c}_0 = \tilde{c}_N = 2$  and  $\tilde{c}_j = 1$  for  $1 \leq j \leq N-1$ . The higher-order differentiation matrix is just the matrix multiplication of the lower ones, *i.e.*,  $d^m/d\tilde{Z}^m|_{\tilde{Z}=\tilde{Z}_k} \approx \mathbf{D}^{(m)} = [\mathbf{D}^{(1)}]^m = \mathbf{D}^{(1)} \times \mathbf{D}^{(1)} \times \dots \times \mathbf{D}^{(1)}$ .

As for the time integration, a second-order backward-difference formula is used for the flow equations. Let the time step be  $\Delta T$ , and a subscript denote the functional value at the corresponding grid point, while a superscript indicates the time step. Then, equations (5.3a) and (5.3b) are discretized as:

$$Q_j^{n+1} = 1 - \int_{-1}^{\tilde{Z}_j} \frac{1}{2} \beta (\dot{U}_Y)^{n+1} d\tilde{Z}, \quad (\text{SM.1.3})$$

$$P_j^{n+1} = \int_1^{\tilde{Z}_j} \frac{1}{2} \left\{ -\frac{\hat{R}e}{\bar{H}^{n+1}} \frac{3Q^{n+1} - 4Q^n + Q^{n-1}}{2\Delta T} - \frac{6\hat{R}e}{5\bar{H}^{n+1}} 2D^{(1)} \frac{(Q^{n+1})^2}{\bar{H}^{n+1}} - \frac{12Q^{n+1}}{(\bar{H}^{n+1})^3} \right\} d\tilde{Z}. \quad (\text{SM.1.4})$$

Both of these equations have been integrated in space, with  $Q_0 \equiv Q|_{Z=0} = 1$  imposed in equation (SM.1.3) and  $P_N \equiv P|_{Z=1} = 0$  imposed in equation (SM.1.4). The integral is to be evaluated numerically using the trapezoidal rule. Note  $d\tilde{Z} = 2dZ$  due to the change of variables introduced above. Also, in equation (SM.1.3),  $\dot{U}_Y$  denotes the velocity of the interface, which can be obtained from equation (SM.1.7b) below.

The so-called Newmark- $\beta$  method is applied to the governing solid equation (4.12). Then, the spatially discretized equation (4.12) is written as

$$\mathbf{M}\ddot{\mathbf{U}}_Y + \mathbf{K}\bar{\mathbf{U}}_Y = \mathbf{P}, \quad (\text{SM.1.5})$$

with

$$\mathbf{M} = \theta_t \mathbf{I}, \quad \mathbf{K} = \mathbf{I} - \theta_t \mathbf{D}^{(2)}. \quad (\text{SM.1.6})$$

Here,  $\theta_t$  is evaluated from equation (4.16). To ensure the accuracy of the numerical integration required to evaluate  $\theta_t$ , the kernel,  $(d\bar{H}/dZ)^2 \approx (2\mathbf{D}^{(1)}\bar{H})^2$ , is interpolated on the finer grid of  $N = 1024$  using the `barycentric_interpolate` subroutine in SciPy. Then, a Gauss-Lobatto quadrature is applied on the finer grids to calculate the integral in equation (4.16).

With the coefficients in equation (SM.1.5) determined, the acceleration, velocity and displacement of the interface are calculated as

$$\ddot{\mathbf{U}}_Y^{n+1} = (\mathbf{M} + \phi_2 \Delta T^2 \mathbf{K})^{-1} \left\{ \mathbf{P}^{n+1} - \mathbf{K} \left[ \bar{\mathbf{U}}_Y^n + \Delta T \dot{\mathbf{U}}_Y^n + \left( \frac{1}{2} - \phi_2 \right) \Delta T^2 \ddot{\mathbf{U}}_Y^n \right] \right\}, \quad (\text{SM.1.7a})$$

$$\dot{\mathbf{U}}_Y^{n+1} = \dot{\mathbf{U}}_Y^n + (1 - \phi_1) \Delta T \ddot{\mathbf{U}}_Y^n + \phi_1 \Delta T \ddot{\mathbf{U}}_Y^{n+1}, \quad (\text{SM.1.7b})$$

$$\bar{\mathbf{U}}_Y^{n+1} = \bar{\mathbf{U}}_Y^n + \Delta T \dot{\mathbf{U}}_Y^n + \left( \frac{1}{2} - \phi_2 \right) \Delta T^2 \ddot{\mathbf{U}}_Y^n + \phi_2 \Delta T^2 \ddot{\mathbf{U}}_Y^{n+1}, \quad (\text{SM.1.7c})$$

where  $\phi_1$  and  $\phi_2$  are two adjustable parameters. The Newmark- $\beta$  scheme is unconditionally stable and second-order accurate if  $\phi_1 = 1/2$  and  $\phi_2 = 1/4$ . However, to damp out numerically-induced high-frequency oscillations,  $\phi_1 > 1/2$  is usually needed (Subbaraj and Dokainish, 1989). In our simulations, we use  $\phi_1 = 1.0$  and  $\phi_2 = 0.5625$ .

Finally, the discretized interface equation (4.10) is simply

$$\bar{H}_j^{n+1} = 1 + \beta (\bar{U}_Y)_j^{n+1}. \quad (\text{SM.1.8})$$

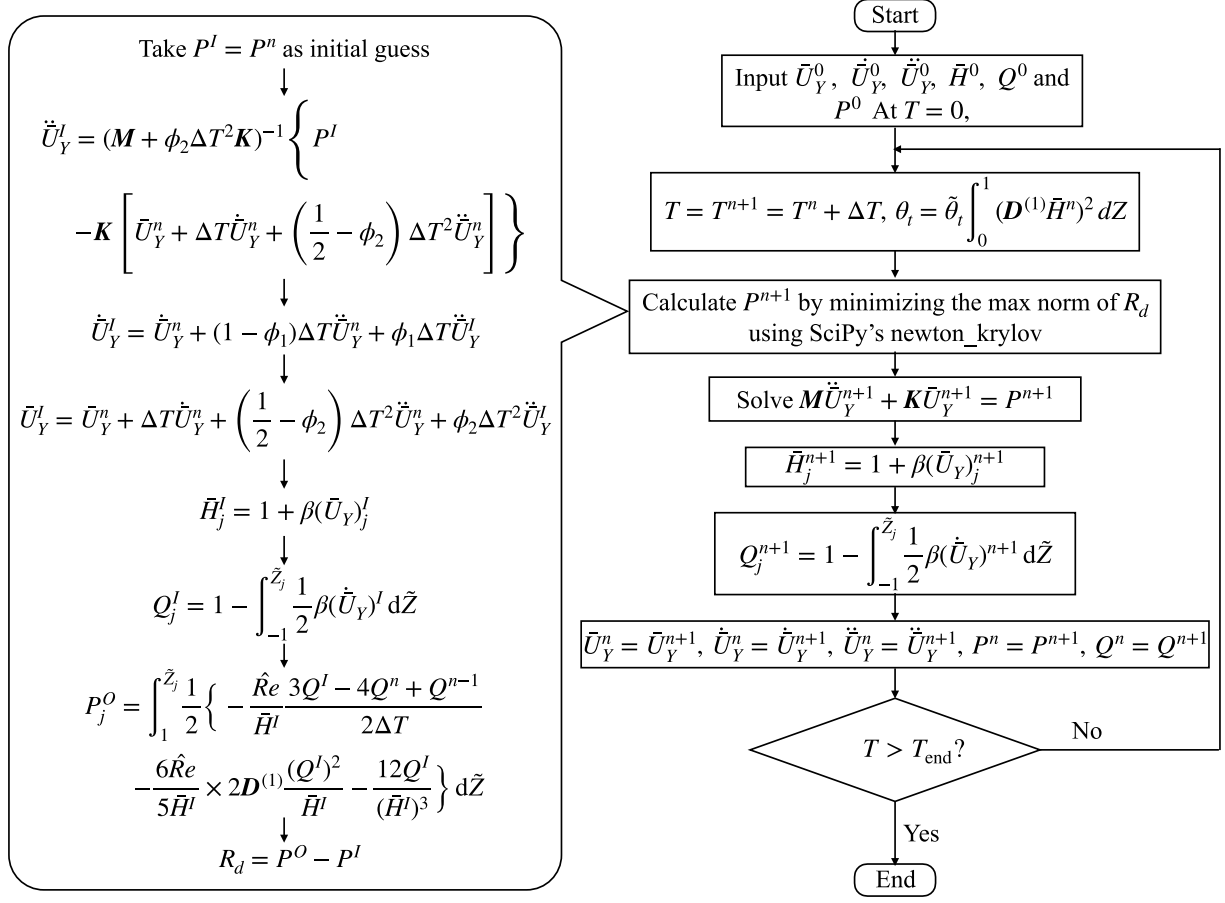


Figure 1: Flow chart of the numerical scheme for the dynamic simulations. To the left of the cell where SciPy's `newton_krylov` solver is called, the details of the construction of the residual,  $R_d$ , is shown. The superscript  $I$  indicates that the quantity is calculated based on  $P^I$ .

### SM.1.1 Steady-state simulation

As mentioned in the main text, the case with given constant tension can be easily solved using ScPpy's `solve_bvp`. However, in the case of the deformation-dependent tension, since  $\theta_t$  is unknown, `solve_bvp` is not as robust and usually has difficulty reaching convergence. Instead, SciPy's `newton_krylov` method is applied to resolve the steady-state solution.

At steady state, all of the terms involving  $\Delta T$  can be neglected. Further, we drop the subscripts on the spatial discretizations for convenience. Then, equations (SM.1.3), (SM.1.4), (SM.1.5) and (SM.1.8) comprise a nonlinear algebraic problem. Then, given  $\bar{U}_Y$ , equations (SM.1.8) and (SM.1.4) allow us to evaluate the pressure, denoted as  $P^F$ . At the same time, equation (SM.1.5) can also be used to evaluate the pressure, denote as  $P^S$ . Now, we define a residual as

$$R_s = P^F - P^S. \quad (\text{SM.1.9})$$

SciPy's `newton_krylov` solver is used to minimize the max-norm of  $R_s$ , which yields an approximate evaluation for  $\bar{U}_Y$  at steady state. The tolerance used was  $6 \times 10^{-6}$ .

With  $\bar{U}_Y$  obtained,  $\theta_t$  is calculated from equation (4.16) using the Gauss-Lobatto quadrature, as discussed before. The steady-state solution is then validated with `solve_bvp` by solving equation (6.1), where both the initial guess and  $\theta_t$  are based on the outputs of `newton_krylov`.

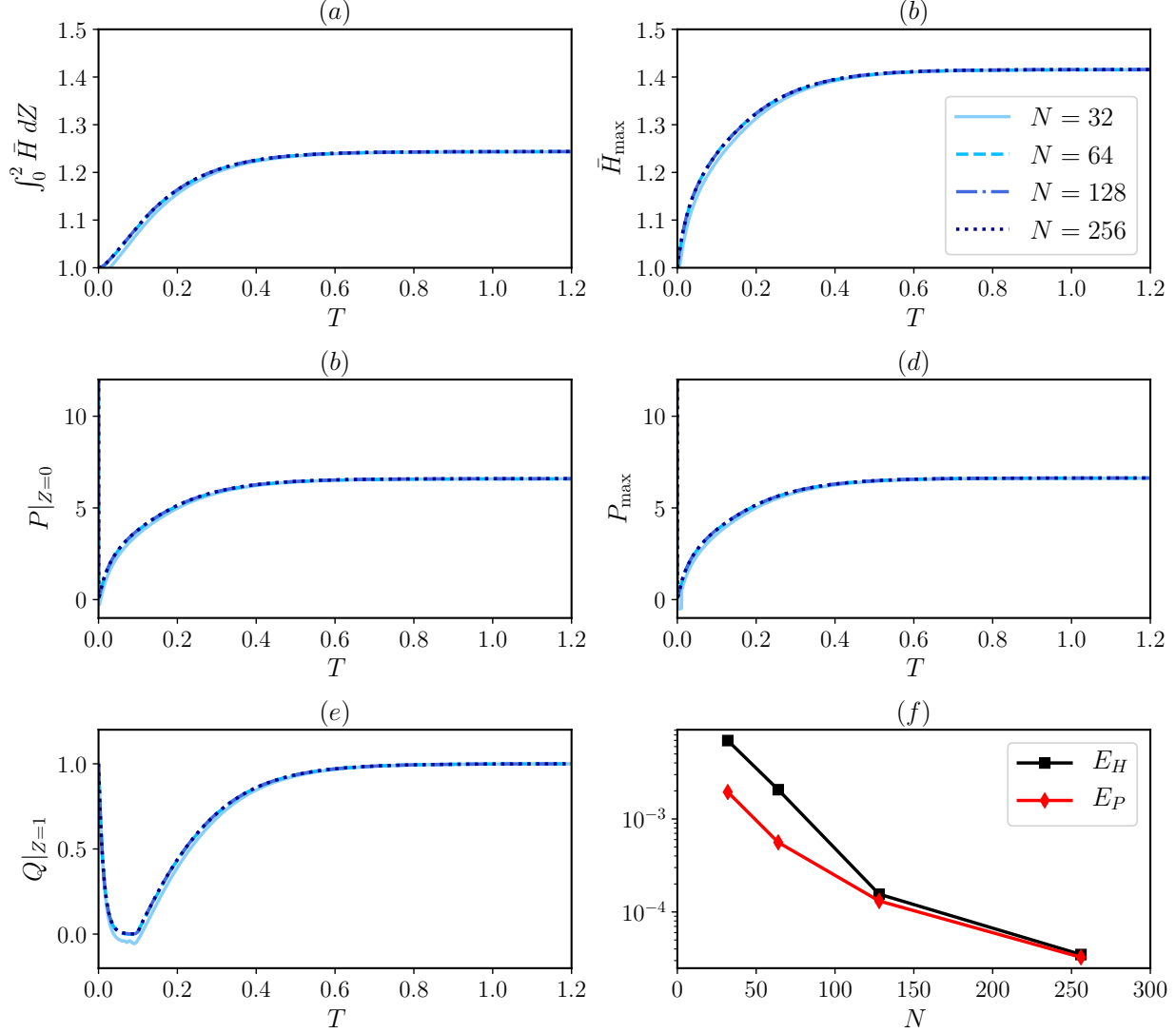


Figure 2: Grid independence study on the dynamic simulations of FSI in the microchannel with  $E = 2$  MPa under a flow rate of  $q = 1500 \mu\text{L min}^{-1}$  (case C4). The time histories of the representative quantities in the system are shown in panels (a) to (e). Panel (f) shows the two-norm of the difference between the simulated steady state solution and the “exact” solution, which is computed from the steady simulation with  $N = 2048$  Gauss-Lobatto points using the scheme described in section SM.1.1. The tolerance used in SciPy’s `newton_krylov` was  $10^{-8}$ . The errors  $E_H$  and  $E_P$  are computed via equation (SM.1.11).

### SM.1.2 Dynamic simulation

The dynamic problem is solved in a similar manner. At each time step, the nonlinear system of equations (SM.1.3), (SM.1.4), (SM.1.5) and (SM.1.8) must be solved. However, to get the Newmark- $\beta$  time integration (SM.1.7) involved, the residual,  $R_d$ , is defined with the pressure as the input, denoted as  $P^I$ . Then, starting from equation (SM.1.5), solved with the scheme (SM.1.7),  $\bar{U}_Y$  and  $\dot{\bar{U}}_Y$  are obtained. Then,  $\bar{H}$  and  $Q$  are evaluated from equations (SM.1.8) and (SM.1.3), respectively. Equation (SM.1.4) gives another evaluation of the pressure, denoted as,  $P^O$ . The residual is thus evaluated as

$$R_d = P^O - P^I. \quad (\text{SM.1.10})$$

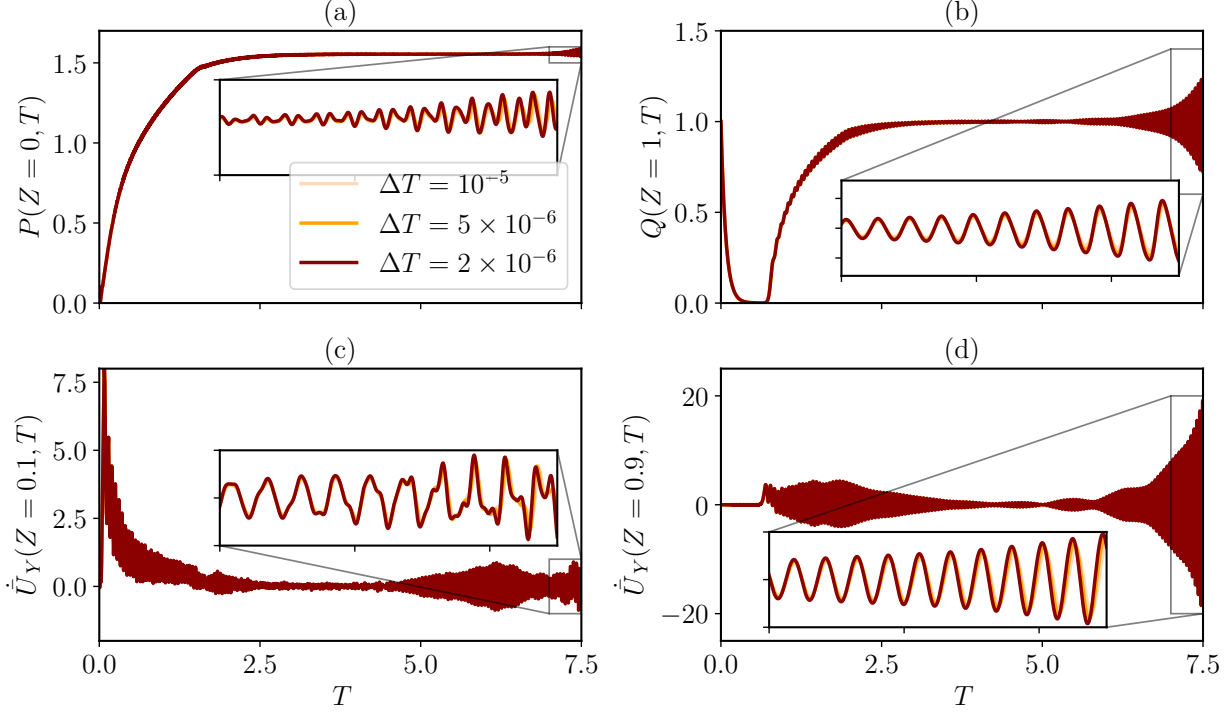


Figure 3: Time histories of (a) inlet pressure  $P(0, T)$ , (b) outlet flow rate  $Q(1, T)$ , the vertical velocity  $\dot{U}_Y$  of the fluid–solid interface at (c)  $Z = 0.1$  and (d)  $Z = 0.9$ . All panels are for case C3 but using different time step sizes  $\Delta T$ . The spatial grid is fixed to have  $N = 128$  nodes.

At each time step, SciPy’s `newton_krylov` is used to minimize the max-norm of  $R_d$ . The details of this numerical procedure are summarized in the flow chart in figure 1.

Note that at time step  $n + 1$ ,  $\theta_t$  is evaluated as  $\theta_t = \tilde{\theta}_t \int_0^1 (\mathbf{D}^{(1)} \bar{H}^n)^2 dZ$ . The integral is approximated using the Gauss–Lobatto quadrature after interpolating the kernel on the finer grid of  $N = 1024$ . Here, we use  $\bar{H}^n$  instead of  $\bar{H}^{n+1}$  in order to avoid another nonlinear problem requiring “internal iterations” on  $\theta_t^{n+1}$ . We have verified that the results using  $\bar{H}^n$  instead of  $\bar{H}^{n+1}$  do not differ from those evaluated based on more involved method using  $\bar{H}^{n+1}$ .

### SM.1.2.1 Grid independence study

Next, we verify the grid independence of the numerical results shown in the main text. The case chosen to perform the grid independence study is C4 from table 5 (corresponding to  $E = 2$  MPa and  $q = 1500$   $\mu\text{L min}^{-1}$ ). For case C4, we have shown in section 7 that the inflated steady state is linearly stable to infinitesimal perturbations. If the flat initial condition (5.6) is used, then the system will reach the steady state eventually.

The end time for the simulation is  $T_{\text{end}} = 2.0$ . However, for the clarity of the presentation, only the results between  $T = 0$  and  $T = 1.2$  are shown. Furthermore, the ratio of the smallest grid size to the time step is fixed for every simulation. Since the smallest spacing of the Gauss–Lobatto grid points goes as  $\mathcal{O}(N^{-2})$ , then as  $N$  is doubled,  $\Delta T$  is decreased by a factor 4 accordingly. The time step for  $N = 32$  is  $\Delta T = 4 \times 10^{-4}$ . As shown figure 2(a) and (e), all of the representative quantities agree well with each other as  $\Delta T$  is refined, except on the courses grid with  $N = 32$ ,

After the simulation has reached  $T = T_{\text{end}}$ , the deformed interface shape,  $\bar{H}^{\text{end}}(Z)$ , and the pressure distribution within the channel,  $P^{\text{end}}(Z)$  are compared with an “exact” steady-state solution. The latter are denoted as  $\bar{H}^e(Z)$  and  $P^e(Z)$ , respectively. The “exact” solution is taken to be the steady state of the simulation with  $N = 2048$ , and tolerance for SciPy’s `newton_krylov` set to  $10^{-8}$ . We define two  $L^2$ -norm

based error estimates:

$$E_H = \left( \frac{1}{2} \sum_{j=1}^{N-1} (\bar{H}_j^{\text{end}} - \bar{H}_j^e) \mathfrak{w} \sqrt{1 - \tilde{Z}_j^2} \right)^{1/2}, \quad (\text{SM.1.11a})$$

$$E_P = \left( \frac{1}{2} \sum_{j=1}^{N-1} (P_j^{\text{end}} - P_j^e) \mathfrak{w} \sqrt{1 - \tilde{Z}_j^2} \right)^{1/2}, \quad (\text{SM.1.11b})$$

which are written in the discrete form using the Gauss–Lobatto quadrature. Here,  $\mathfrak{w} = \pi/N$  are the weights, and we choose  $N = 2048$ . Figure 2(f) shows that the error decreases with the increase of  $N$ . The cases of  $N = 32, 64$  and  $128$  even display an exponential decay for  $E_H$ . However, since the “exact” solution is not really exact, both error estimates tend to “saturate” for  $N = 256$ .

As for the linearly unstable cases, the errors defined in equation (SM.1.11) are not applicable because the system will not reach steady state. In these cases, each simulation is tested with different time step sizes, and only the converged results are shown. The spatial grid is typically fixed as  $N = 128$  for satisfactory accuracy (as shown in figure 2). One example for case C3 is shown in figure 3. In panel (c) and (d), the vertical velocity of the fluid–solid interface is obtained as follows. First, we substitute the simulated  $\bar{H}$  into equation (5.1) to obtain  $V_Z^{2D}$ . Then, we compute  $V_Y^{2D}$  based on conservation of mass, *i.e.*,  $\partial V_Z^{2D}/\partial Z + \partial V_Y^{2D}/\partial Y = 0$ . Lastly, we obtain  $\dot{U}_Y = \beta^{-1} V_Y^{2D}|_{Y=\bar{H}}$  using equations (5.2) and (4.10). The actual simulation time is longer than the time window shown for each case. However, it is observed that after a certain  $T$ , the results with different time step sizes begin to diverge, indicating this nonlinear 1D FSI model’s dynamic behavior may be chaotic. Understanding such an interesting possibility is beyond of the scope of the current work.

## SM.2 A Chebyshev pseudospectral method for the generalized eigenvalue problem

We solve the generalized eigenvalue problem (7.4) using the approach proposed by Inamdar et al. (2020). However, since the boundary conditions for equation (7.4) are different from the boundary conditions of Inamdar et al. (2020), we employ another modified Lagrange polynomial basis, now written as

$$\tilde{Q}(\tilde{Z}) \approx (1 + \tilde{Z}) \sum_{j=1}^N \tilde{Q}_j \frac{\ell_j(\tilde{Z})}{1 + \tilde{Z}_j}, \quad \tilde{H}(\tilde{Z}) \approx \sum_{j=1}^{N-1} \tilde{H}_j \ell_j(\tilde{Z}) + \tilde{H}_N (1 - \tilde{Z}^2). \quad (\text{SM.2.1})$$

It is easy to check that  $\tilde{Q}(\tilde{Z}_j) = \tilde{Q}_j$  and  $\tilde{H}(\tilde{Z}_j) = \tilde{H}_j$ , except that  $\tilde{H}(\tilde{Z}_N) = 0 \neq \tilde{H}_N$ , meaning that  $\tilde{Q}_j$  and  $\tilde{H}_j$  are the collocated function values;  $\tilde{H}_N$  is introduced ensure the satisfaction of the boundary condition. Also note  $j$  starts from 1 instead of 0, because equation (SM.2.1) has already satisfied the conditions that  $\tilde{Q} = d\tilde{Q}/d\tilde{Z} = 0$  at  $\tilde{Z} = -1$ , and  $\tilde{H} = 0$  at  $\tilde{Z} = \pm 1$ . The two remaining boundary conditions at  $\tilde{Z} = 1$  in equation (7.6) are enforced manually.

Next, the generalized eigenvalue problem (7.4) is collocated at the Gauss–Lobatto points from  $j = 1, 2, \dots, N-1$ , with the unsatisfied boundary conditions enforced at  $j = N$ . This approach gives rise to the  $2N \times 2N$  matrices  $\mathbf{A}$  and  $\mathbf{B}$  in equation (7.4). Due to the imposition of the boundary conditions at  $\tilde{Z} = 1$ ,  $\mathbf{B}$  is singular. Thus, we invert  $\mathbf{A}$  to obtain a regular eigenvalue problem,  $\mathbf{A}^{-1} \mathbf{B} \boldsymbol{\psi} = (i\omega_G)^{-1} \boldsymbol{\psi}$ , which can be solved using SciPy’s `eig`.

Finally, to filter out any spurious modes, each calculation has been performed with  $N = 600$  and  $N = 800$  grid points and cross-checked. Only the converged modes are reported in the text.